

# A numerical simulation of the evolution and fate of a FRI jet. The case of 3C 31

M. Perucho,<sup>1</sup> J.-M.<sup>a</sup> Martí,<sup>2</sup>

<sup>1</sup>Max-Planck-Institut für Radioastronomie, Auf dem Hügel 69, 53121 Bonn, Germany

<sup>2</sup>Departament d'Astronomia i Astrofísica, Universitat de València, Dr. Moliner 50, 46100 Burjassot (València), Spain

Released 2007 XXXXX XX

## ABSTRACT

The evolution of FRI jets has been long studied in the framework of the FRI-FRII dichotomy. The present paradigm consists of the expansion of overpressured jets in the ambient medium and the generation of standing recollimation shocks, followed by mass entrainment from the external medium that decelerates the jets to subsonic speeds. In this paper, we test the present theoretical and observational models via a relativistic numerical simulation of the jets in the radio galaxy 3C 31. We use the parameters derived from the modelling presented by Laing & Bridle (2002a,b) as input parameters for the simulation of the evolution of the source, thus assuming that they have not varied over the lifetime of the source. We simulate about 10 % of the total lifetime of the jets in 3C 31. Realistic density and pressure gradients for the atmosphere are used. The simulation includes an equation of state for a two-component relativistic gas that allows a separate treatment of leptonic and baryonic matter. We compare our results with the modelling of the observational data of the source. Our results show that the bow shock evolves self-similarly at a quasi-constant speed, with slight deceleration by the end of the simulation, in agreement with recent X-ray observations that show the presence of bow shocks in FRI sources. The jet expands until it becomes underpressured with respect to the ambient medium, and then recollimates. Subsequent oscillations around pressure equilibrium and generation of standing shocks lead to the mass loading and disruption of the jet flow. We derive an estimate for the minimum age of the source of  $t > 1.10^8$  yrs, which may imply continuous activity of 3C 31 since the triggering of its activity. The simulation shows that weak CSS sources may be the young counterparts of FRIs. We conclude that the observed properties of the jets in 3C 31 are basically recovered by the standing shock scenario.

**Key words:** galaxies: individual: 3C 31 – galaxies: active – galaxies: nuclei – galaxies: jets – radio continuum: galaxies

## 1 INTRODUCTION

The morphology and evolution of jets in low-power radiogalaxies, i.e., FRI radiogalaxies in Fanaroff & Rileys (1974) classification, have been addressed by a number of authors, from theoretical (e.g., Bicknell 1984, 1994; Komissarov 1990a,b, 1994; De Young 1993), numerical (e.g., De Young 1986; Bowman et al. 1996) and observational (e.g., Parma et al. 2002; Laing & Bridle 2002a,b) points of view. FRI jets show bright regions close to the core dimming into diffuse emission at kiloparsec scales. The jets in FRI sources are relativistic at the parsec scales (see, e.g., Laing 1993, 1996), but decelerate between the inner regions and the kiloparsec scales (see, e.g., Laing 1996).

The theoretical paradigm for the evolution of jets in FRI sources (Bicknell 1984; Laing 1993, 1996) comprises the expansion of an overpressured jet, followed by the generation of shocks due to subsequent compressions and expansions around pressure equilibrium; the jet is decelerated in these shocks and entrains the external medium through turbulent mixing. The last stage of

the evolution, when the jet has already been decelerated to subsonic speeds, is dominated by turbulence. Two main processes for the entrainment of the ambient medium in the jets have been invoked and studied in the literature: 1) entrainment through mixing in a turbulent shear layer between the jet and the medium, and 2) entrainment from stellar mass losses. Komissarov (1990a,b) developed a theoretical model for the mass entrainment at the jet boundary and made steady-state numerical calculations, succeeding in explaining the main features of FRI jets. A series of authors have concentrated on this topic. De Young (1986) and Bicknell (1994) studied the entrainment in jets. De Young (1993) studied the importance of a sufficiently dense environment in decelerating jets through entrainment. Komissarov (1994) studied the mass load of a leptonic jet by stellar winds, concluding that this entrainment can be very important for the process of deceleration. Bowman et al. (1996) performed a series of steady-state numerical simulations using an equation of state for a two-component relativistic gas (see also Bowman 1994) and including a term for the entrainment of the

stellar mass loss in the code according to the model of Komissarov (1994).

Laing & Bridle (2002a,b) –LB02a,b from now on– presented a model which accurately describes the kinematics and dynamics of the jets in the FRI radiogalaxy 3C 31, mapping the emission and magnetic fields of the jets. In LB02a, the observed brightness and polarization distributions were fitted by modelling the velocity, synchrotron emissivity and ordering of the magnetic field. In LB02b, a dynamical model was presented based on the results of LB02a and estimates for external pressure and density profiles from *Chandra* (Hardcastle et al. 2002), applying conservation of particles, momentum and energy, and assuming that the jets are in pressure equilibrium with the external medium at large distances from the nucleus. Laing & Bridle (2004) studied the validity of so-called adiabatic models in explaining the structure of the magnetic and velocity fields, and the brightness and polarization distributions in the jets of 3C 31. In these models, the radiating particles are supposed to be accelerated before entering the region of interest and then lose energy only by adiabatic processes. The authors concluded that the adiabatic models give a good description of the outer regions of the jet, whereas closer to the nucleus, the jet shows a non-adiabatic behavior. Their fit to the data is inferior to that of the free models of LB02a, but is obtained with fewer free parameters.

In this paper, we present the results from a relativistic, purely hydrodynamical simulation with input parameters taken from LB02a,b. It is not clear if the magnetic field in the jets of 3C 31 is dynamically important, although it seems, from the results obtained by LB02a,b, that it is close to equipartition. However, we will assume in this work that the magnetic field is not important for the dynamics of the problem. This assumption remains to be checked by future relativistic magnetohydrodynamic simulations. Our aim is to compare the results from the simulation with those from observations and modelling. We also address the problem of the jet evolution and young counterparts to FRI jets. The nature of compact radio-sources and their relation with large scale jets has been studied during the last years. Compact Symmetric Objects (CSO), as a morphological subclass of Giga-hertz Peaked Spectrum sources (GPS) and Compact Steep Spectrum sources (CSS), are understood as the young counterparts of FRII jets (e.g., Fanti et al. 1995; Perucho & Martí 2002). However, there is still some debate on the compact radio sources that could be the young FRIs. Drake et al. (2004) and Kunert-Bajraszewska et al. (2005) have observed low-power CSS from the IRAS sample and the FIRST survey, respectively. Drake et al. (2004) proposed these weak CSS sources as the possible young counterparts of FRI jets. We study this possibility in this work.

To our knowledge this is the first work to present long term relativistic simulations of FRI jets. In contrast, the evolution of FRII jets has been addressed by several authors (see, e.g., Komissarov & Falle 1998; Scheck et al. 2002; Krause & Camenzind 2003; Krause 2005). Our work covers a parameter space complementary to that used in Scheck et al. (2002), who discussed the dependence of the morphology and dynamics of jets on their composition, using the same equation of state as used here.

The plan of the paper is as follows. In Section 2, we present the setup of our simulation. In Section 3 we summarize the main results of the simulation, and we compare these results with new simulations performed in order to test different evolutionary scenarios by changing the initial conditions. In Section 4 we discuss the main results of the work, and we present the conclusions of the paper in Section 5.

## 2 SETUP OF THE NUMERICAL SIMULATION

### 2.1 The model of Laing & Bridle

The numerical simulation presented in this paper is based on the work by Laing & Bridle (LB02a,b), as stated in the Introduction. In this paragraph we review their main assumptions and conclusions. In the modelling presented in LB02a the jet and counter-jet are assumed to be identical, antiparallel, axisymmetric and stationary, and the differences between them are assumed to be due to relativistic aberration. The models are designed to fit the observed brightness and polarization distributions (assuming optically thin emission), taking into account Doppler boosting effects and relying on simple prescriptions for the variations of the flow velocity, synchrotron emissivity and magnetic-field structure within the jet. The rotation of the line of sight relative to the magnetic field structure between the emitted and the observed frames is also taken into account. The model focuses on the region enclosing the inner 12 kpc of the jets, which is split in three parts: the inner region (from 0 to 1.1 kpc, or from 0 to 2.5 arcsec), the flaring region (from 1.1 to 3.5 kpc, or from 2.5 to 8.3 arcsec) and the outer region (from 3.5 to 12 kpc, or from 8.3 to 28.3 arcsec). The linear distances are calculated assuming a Hubble constant  $H_0 = 70 \text{ km s}^{-1} \text{ Mpc}^{-1}$ , taking the redshift of the parent galaxy of 3C 31 (NGC 383,  $z = 0.0169$ ) and a viewing angle of  $52^\circ$ . This modelling has been extended to other FRI sources (e.g., NGC 315 and 3C 296, Canvin et al. 2005; Laing et al. 2006). In LB02b, the authors present a dynamical model for the jet, based on: 1) the results obtained in LB02a, 2) estimates of pressure and density profiles from *Chandra* and *ROSAT* (Hardcastle et al. 2002; Komossa & Boehringer 1999), 3) the conservation of particles, momentum and energy, 4) the assumption that the jets are in pressure equilibrium with the external medium at large distances from the nucleus, and 5) the momentum flux being  $\Pi = \Phi/c$ , where  $\Phi$  is the energy flux (a good approximation for light, hot and/or relativistic jets). The model is *quasi-one-dimensional*, as, although the widening of the jet is considered, only the axial velocities are used in the analysis. The authors conclude that after the expansion of the jet in the inner region, the jet flow is overpressured and decelerated at the beginning of the flaring region. In this region, they find local minima of pressure and density and maxima in the Mach number and entrainment rate. At the end of the flaring region, the jets are slightly underpressured but close to pressure equilibrium with the ambient medium. Changes in the outer region are smooth, with almost constant density and monotonically increasing entrainment rate. The Mach number in the outer region is  $\sim 1 - 2$ . Comparison of the jet density with the number of radiating particles required by the observed synchrotron emissivity lead the authors to conclude that the jet is probably initially composed of a pair plasma ( $e^- - e^+$ ), and mass-loaded with baryons inside the galaxy. This mass load is attributed dominantly to stellar wind material. The exact origin of the majority of the gas entrained by the jets is, however, still uncertain.

### 2.2 Setup

The numerical simulation was performed using a finite-difference code based on a high-resolution shock-capturing scheme which solves the equations of relativistic hydrodynamics in two dimensions written in conservation form (Martí et al. 1997). The code is parallelized using OMP directives and it has been modified in order to include the equation of state for relativistic Boltzmann gases (Synge 1957; Falle & Komissarov 1996, , and Appendix A in this

paper) with the routines used in the simulations of Scheck et al. (2002). The use of this equation of state allows us to distinguish electrons, positrons and protons in the simulation. Under the assumption of charge neutrality, only one conservation equation (for example, that for the evolution of the leptonic density) must be added in order to know the composition of the fluid at each computational cell. The integration of this extra equation together with the use of the Sygne equation of state (involving the computation of Bessel functions) increases the computational time per iteration by  $\sim 50\%$  with respect to the case of the one component, ideal gas equation of state (Scheck et al. 2002).

The equations of relativistic hydrodynamics in conservation form, which are solved by the code, assuming axisymmetry and in two-dimensional cylindrical coordinates  $(R, z)$ , are the following (we use units in which the speed of light is set to 1):

$$\frac{\partial \mathbf{U}}{\partial t} + \frac{1}{R} \frac{\partial R \mathbf{F}^R}{\partial R} + \frac{\partial \mathbf{F}^z}{\partial z} = \mathbf{S}, \quad (1)$$

with the vector of unknowns

$$\mathbf{U} = (D, D_l, S^R, S^z, \tau)^T, \quad (2)$$

fluxes

$$\mathbf{F}^R = (Dv^R, D_l v^R, S^R v^R + p, S^z v^R, S^R - Dv^R)^T, \quad (3)$$

$$\mathbf{F}^z = (Dv^z, D_l v^z, S^R v^z, S^z v^z + p, S^z - Dv^z)^T, \quad (4)$$

and source terms

$$\mathbf{S} = (0, 0, p/R + g^R, g^z, v^R g^R + v^z g^z)^T. \quad (5)$$

The five unknowns  $D, D_l, S^R, S^z$  and  $\tau$  refer to the densities of five conserved quantities, namely the total and leptonic rest masses, the radial and axial components of the momentum, and the energy (excluding rest mass energy). They are all measured in the laboratory frame, and are related to the quantities in the local rest frame of the fluid (primitive variables) according to

$$D = \rho W, \quad (6)$$

$$D_l = \rho_l W, \quad (7)$$

$$S^{R,z} = \rho h W^2 v^{R,z}, \quad (8)$$

$$\tau = \rho h W^2 - p - D, \quad (9)$$

where  $\rho$  and  $\rho_l$  are the total and the leptonic rest mass density, respectively,  $v^{R,z}$  are the components of the velocity of the fluid,  $W$  is the Lorentz factor ( $W = 1/\sqrt{1 - v^i v_i}$ , where summation over repeated indices is implied), and  $h$  is the specific enthalpy defined as

$$h = 1 + \varepsilon + p/\rho, \quad (10)$$

where  $\varepsilon$  is the specific internal energy and  $p$  is the pressure. Finally,  $g^R, g^z$  appearing in the definition of the source vector, eq. (5), are the components of an external force that keeps the atmosphere in equilibrium (see below). The system (1) is closed by means of the Sygne equation of state described in Appendix A.

The code also integrates an equation for the jet mass fraction,  $f$ . This quantity, set to 1 for the injected beam material and 0 otherwise, is used as a tracer of the jet material through the grid and allows to study phenomena like the entrainment of ambient material in the beam and the mixing in the cocoon.

The medium in which the jet is injected consists of a decreas-

ing density atmosphere composed of Hydrogen<sup>1</sup>. The dynamical equilibrium of the atmosphere is attained by introducing an external force which compensates initial pressure gradients in the radial and axial directions. The profile for the number density of such a medium is (Hardcastle et al. 2002):

$$n_{ext}(r) = n_c \left(1 + \frac{r^2}{r_c^2}\right)^{-3\beta_{atm,c}/2} + n_g \left(1 + \frac{r^2}{r_g^2}\right)^{-3\beta_{atm,g}/2}, \quad (11)$$

where  $r$  is the spherical radial coordinate,  $n_c$  and  $n_g$  are the core densities of the galaxy and the surrounding group,  $r_c$  and  $r_g$  are the radii of those cores, and  $\beta_{atm,c}$  and  $\beta_{atm,g}$  are the exponents giving the profile for each medium. The temperature profile is:

$$T = T_c + (T_g - T_c) \frac{r}{r_m} \quad (r < r_m) \\ T = T_g \quad (r \geq r_m), \quad (12)$$

with  $r_m = 7.8$  kpc. The pressure is derived from the following equation of state:

$$P_{ext} = \frac{k_B T}{\mu X} n_{ext}(r), \quad (13)$$

where  $\mu$  is the mass per particle in a.m.u. ( $\mu = 0.5$  in our case, cf. 0.6 in LB02b),  $X$  is the abundance of hydrogen by mass ( $X = 1$  here, cf. 0.74 in LB02b). In Table 1 we reproduce Table 1 in LB02b, where the parameters for the equations above are listed. The initial profiles for ambient medium pressure and density along the axis of the jet are plotted in Fig. 1.

The numerical code units are the jet radius ( $R_j$ ), the speed of light ( $c$ ) and the density of the ambient medium at injection ( $\rho_{a,c}$ ). Thus, the appropriate unit transformations are performed in the code from physical to code units.

The simulation was performed in cylindrical coordinates with axial symmetry, i.e., only one half of the jet is computed. The grid involved  $2880 \times 1800$  cells, with a resolution of 8 cells/ $R_j$  in the axial direction up to  $300 R_j$ , plus an extended grid with geometrically increasing cell size (up to  $450 R_j$ ), and 16 cells/ $R_j$  in the radial direction up to  $100 R_j$ , plus an extended grid (also with geometrically increasing cell size) up to  $200 R_j$ . Outflow boundary conditions were used at the end of the grid in the axial direction and also far from the jet axis in the radial direction. Reflecting boundary conditions were taken for the jet axis in order to account for the cylindrical symmetry.

Injection of the jet in the atmosphere is done at  $r = 500$  pc, the point where the modelling of the jet in LB02b starts. The radius of the jet at that point is calculated from the opening angle of  $6.7^\circ$  given for the jet in LB02a ( $R_j = 60$  pc). The uniform grid is then  $17.5 \text{ kpc} \times 6 \text{ kpc}$ , and, with the extended grid,  $26.25 \text{ kpc} \times 12 \text{ kpc}$ .

The jet is injected with a speed  $v_j = 0.87 c$  (jet Lorentz factor,  $W_j \sim 2$ ), internal relativistic Mach number  $M_j = 2.5$ , temperature  $T_j = 4.1 \cdot 10^9 \text{ K}$ , density ratio with the external medium  $\eta = 1 \cdot 10^{-5}$ , purely leptonic composition ( $X_l = 1.0$ ), and over-pressured by a factor 7.8 with respect to the ambient medium. In Table 2 we give the complete list of parameters. The parameters given for the ambient medium at injection are calculated for  $r = 500$  pc (this is the reason for differences between Table 1

<sup>1</sup> LB02b use the standard composition with 74% hydrogen, but this treatment would require the inclusion of new populations of particles (in order to account for the remaining 26%) in the code, involving longer computational time, so that we discarded this option.

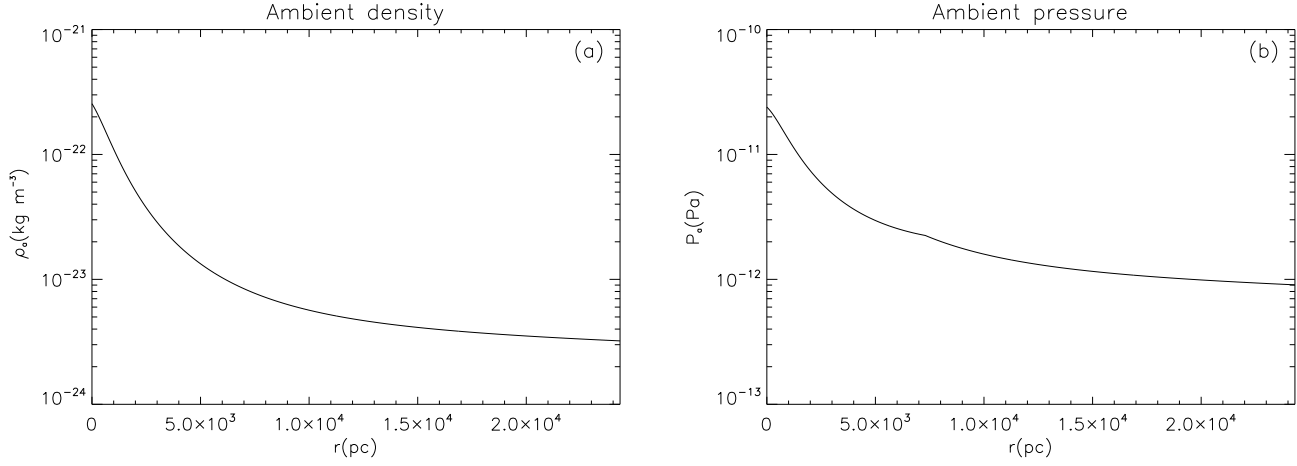


**Figure 1.** Initial profiles of ambient rest mass density (a) and pressure (b).

**Table 1.** Ambient medium parameters (Table 1 in LB02b). Subscripts *c* and *g* refer to the galaxy core and to the surrounding group, respectively.

| Component | Central density                       | Form factor            | Core radius             | Temperature                      |
|-----------|---------------------------------------|------------------------|-------------------------|----------------------------------|
| Galaxy    | $n_c = 1.8 \cdot 10^5 \text{ m}^{-3}$ | $\beta_{atm,c} = 0.73$ | $r_c = 1.2 \text{ kpc}$ | $T_c = 4.9 \cdot 10^6 \text{ K}$ |
| Group     | $n_g = 1.9 \cdot 10^3 \text{ m}^{-3}$ | $\beta_{atm,g} = 0.38$ | $r_g = 52 \text{ kpc}$  | $T_g = 1.7 \cdot 10^7 \text{ K}$ |

**Table 2.** Table of parameters used in the simulation. The one-dimensional velocity estimation given in the Table stands for the theoretical advance velocity of the jet, computed using the equation derived in Martí et al. (1997) for a pressure-matched jet propagating in one dimension (i.e., without sideways expansion) through an homogeneous medium.

|   |  |
|---|--|
| Velocity ( $v_j$ )  | $0.87 c$                               |
| Mach number ( $M_j$ )   | 2.5                                    |
| Temperature ( $T_j$ , jet)  | $4.1 \cdot 10^9 \text{ K}$             |
| Temperature ( $T_c$ , ambient <sup>1</sup> )                        | $5.7 \cdot 10^6 \text{ K}$             |
| Temperature ( $T_g$ , ambient <sup>2</sup> )                        | $1.7 \cdot 10^7 \text{ K}$             |
| Density ( $\rho_j$ , jet)   | $3 \cdot 10^{-27} \text{ kg/m}^3$      |
| Density ( $\rho_{a,c}$ , ambient <sup>1</sup> )                     | $3 \cdot 10^{-22} \text{ kg/m}^3$      |
| Density ratio ( $\eta$ )  | $10^{-5}$                              |
| Leptonic number ( $X_l$ , jet)                                      | 1.0                                    |
| Specific int. energy ( $\varepsilon_j$ , jet)                       | $1.54 c^2$                             |
| Specific int. energy ( $\varepsilon_{a,c}$ , ambient <sup>1</sup> ) | $1.57 \cdot 10^{-6} c^2$               |
| Specific int. energy ( $\varepsilon_{a,g}$ , ambient <sup>2</sup> ) | $4.69 \cdot 10^{-6} c^2$               |
| Pressure ( $P_j$ , jet)   | $6.91 \cdot 10^{-6} \rho_{a,c} c^2$    |
| Pressure ( $P_{a,c}$ , ambient <sup>1</sup> )                       | $8.84 \cdot 10^{-7} \rho_{a,c} c^2$    |
| Pressure ( $P_{a,g}$ , ambient <sup>2</sup> )                       | $3.07 \cdot 10^{-8} \rho_{a,c} c^2$    |
| Pressure ratio ( $P_j/P_{a,c}$ )                                    | 7.8                                    |
| Adiabatic exponent ( $\Gamma_j$ , jet)                              | 1.38                                   |
| Adiabatic exponent ( $\Gamma_a$ , ambient)                          | 1.66                                   |
| 1D velocity estimation ( $v_h^{1d}$ )                               | $9.9 \cdot 10^{-3} c$                  |
| Time unit ( $R_j/c$ )   | $60 \text{ pc}/c \sim 195 \text{ yrs}$ |

<sup>1</sup> and <sup>2</sup> stand for values in the ambient medium at the injection and point furthest from injection in the grid, respectively.

and Table 2). The numbers in this table give an energy flux for the jet of  $\Phi \sim 10^{37} \text{ W}$ , which is very close to the value given in LB02b ( $\Phi = 1.1 \cdot 10^{37} \text{ W}$ ), the difference being due to approximations in variables considered. The quantity  $L_{kin}$  (kinetic luminosity of the jet) used for the simulations in Scheck et al. (2002), where

the authors make a study of the influence of jet composition on its long term evolution, is equivalent to the jet energy flux defined in LB02b. Comparing the value of  $L_{kin}$  in our simulation to that used in Scheck et al. (2002) we use  $L_{kin} \sim 10^{37} \text{ W}$ , on the upper end of the power distribution of FRI sources, whereas in their work the jets have  $L_{kin} \sim 10^{39} \text{ W}$ , appropriate for an FRII source.

## 3 RESULTS

### 3.1 Evolution

#### 3.1.1 Numerical Results

The simulation was run for  $\sim 2000$  hours ( $\sim 83$  days) on eight processors in the SGI Altix computer CERCA, at the *Universitat de València*, corresponding to a source lifetime of  $7.26 \cdot 10^6$  yrs. At the moment when it was stopped, the bow shock of the jet was located at  $\sim 14.5 \text{ kpc}$  from the injection point in the grid, i.e., at  $\sim 15 \text{ kpc}$  from the source. The large amount of computational time needed is a consequence of the small advance speed of a FRI-like source and of the numerical effort invested in the computation of the relativistic equation of state.

Fig. 2 shows panels of the logarithm of rest mass density and Lorentz factor at different times of the first stages of evolution. The compact phase, defined as that in which the source has a linear size smaller than  $5 \text{ kpc}$  can be divided into two main epochs, based on these maps: 1) the *CSO-like* phase, when the source is smaller than  $1 \text{ kpc}$ , and 2) the *weak CSS-like* phase, when the source is between  $1$  and  $5 \text{ kpc}$  long. During the *CSO-like* phase (top panels in Fig. 2), the jet shows a large opening angle, due to overpressure with respect to the ambient medium and a strong Mach disk at its head. Hence the morphology of the source is dominated by a short and featureless beam and a strong hot-spot downstream of the terminal Mach shock. During the *weak CSS-like* phase (mid and bottom

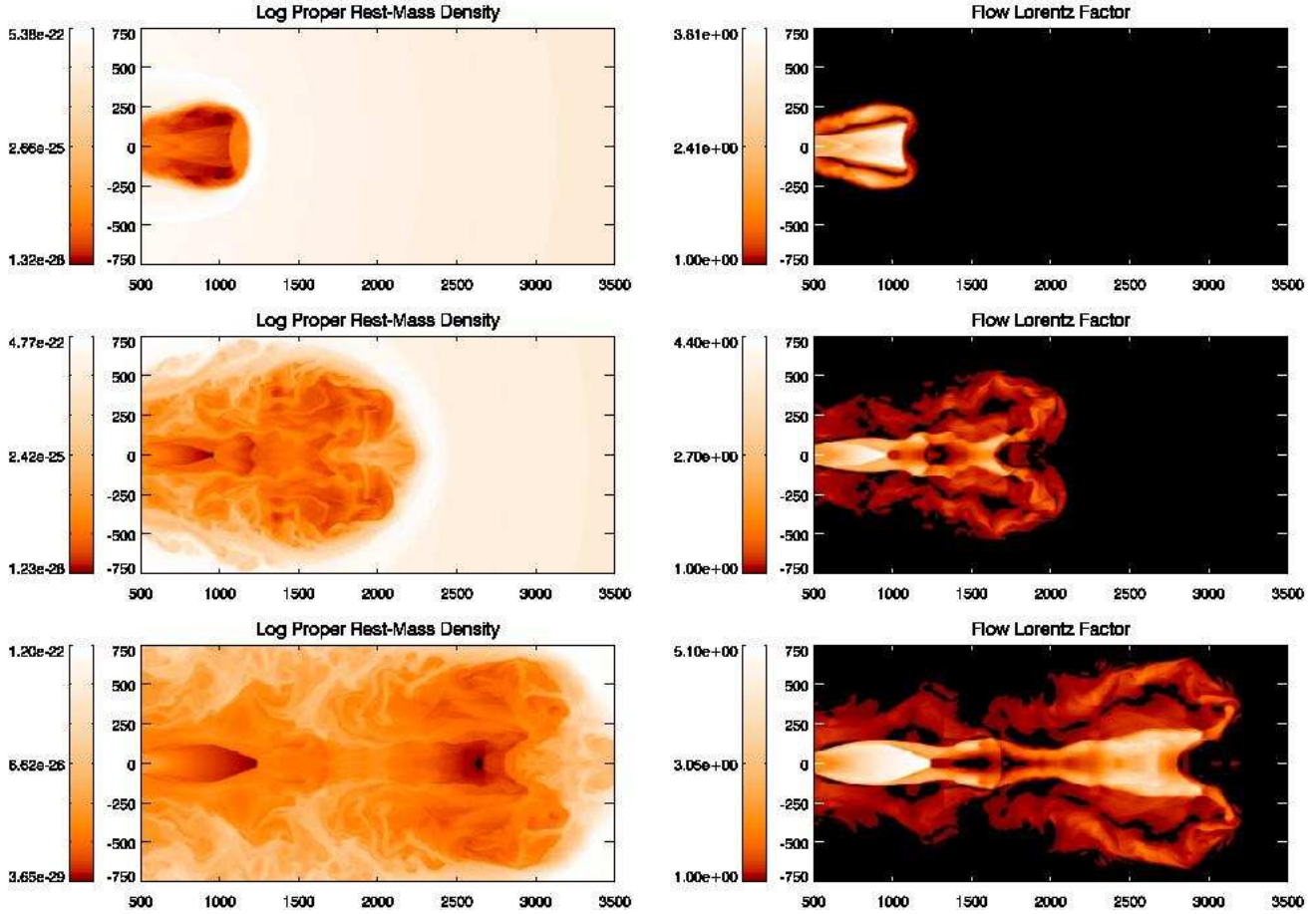


**Figure 2.** Logarithm of rest mass density (left panels) in  $\text{kg/m}^3$  and Lorentz factor (right panels) at three different times ( $2.7 \cdot 10^5$ ,  $8.2 \cdot 10^5$  and  $1.4 \cdot 10^6$  yrs) during the compact phase of the evolution. Coordinates are in parsecs.

panels in Fig. 2), the Mach disk is weaker, as the jet is slowed down in recollimation shocks. The whole structure of the jet appears to be much more irregular during the latter phase. The transition between the phases occurs in the course of the evolution, when the terminal Mach shock disappears for the first time leading to a conical shock, at  $t = 4.3 \cdot 10^5$  yrs, when the linear size of the jet is in the range  $1 - 1.5$  kpc, i.e. in the transition between CSO and CSS phases of young radio sources. The flow dynamics behind the shock then changes affecting the global evolution of the jet. This behaviour was already noted by Scheck et al. (2002) in the context of the early evolution of FRII jets. It is important to remark that the axial symmetry imposed on the simulation affects the internal structure of the jet (internal and terminal shocks) and hence the jet dynamics and advance speed as discussed, e.g., by Aloy et al. (1999). However, for the short times/sizes involved in the previous discussion, the hypothetical three dimensional effects are expected to be negligible.

Fig. 3 shows the evolution of several quantities versus time during the simulation. Fig. 3a shows the position of the bow shock as a function of time. The curve is consistent with a constant-velocity expansion up to  $t = 4.5 \cdot 10^6$  yrs (corresponding source size in the axial direction, 9.5 kpc), and with a decelerating expansion afterwards. Despite the variations, the advance velocity of the bow shock, in Fig. 3c, shows this trend. Initially, the advance speed is  $v_{bs} \sim 7 \cdot 10^{-3} c$ , close to the one-dimensional estimate of the head of the jet for homogeneous ambient medium,  $v_h^{1d} = 9.9 \cdot 10^{-3} c$

(Table 2), but by the end of the simulation, it has decreased to  $v_{bs} < 6 \cdot 10^{-3} c$ . The duration of the phase with constant advance speed is longer than in the case of simulations with a uniform ambient medium (e.g., Scheck et al. 2002) because the deceleration caused by the widening of the jet along the evolution is now approximately balanced by the decrease of the inertia of the ambient medium with distance. As stated in the previous paragraph, three dimensional effects can modify the change of jet advance speed with time. In particular, the *one dimensional phase* can be shortened and phases of acceleration can appear occasionally when the terminal shock changes from planar to oblique. Hence the results discussed in this paragraph must be treated with caution. The pressure behind the bow shock, in Fig. 3b, drops and oscillates until the end of the simulation following the behaviour of the ambient pressure although with a larger instantaneous slope. The effect of deceleration of the bow shock and the increase of temperature in the ambient medium at larger distances to the source combine to give a mild reduction of the Mach number (Fig. 3d) along the evolution, although the shock is still supersonic ( $M_{bs} \sim 2 - 3$ ) by the end of the simulation. Recent works by Kraft et al. (2003) and Croston et al. (2007) have detected the existence of shock waves surrounding the radio lobes of the relatively young ( $t \sim 2 \cdot 10^6$  yrs) FRI jets of Centaurus A and NGC 3801, respectively. The shock waves are revealed by shells of hot interstellar gas emitting in the X-rays. The authors derive Mach numbers between 3 and 8 for these shocks. The ages and Mach numbers obtained in our simu-

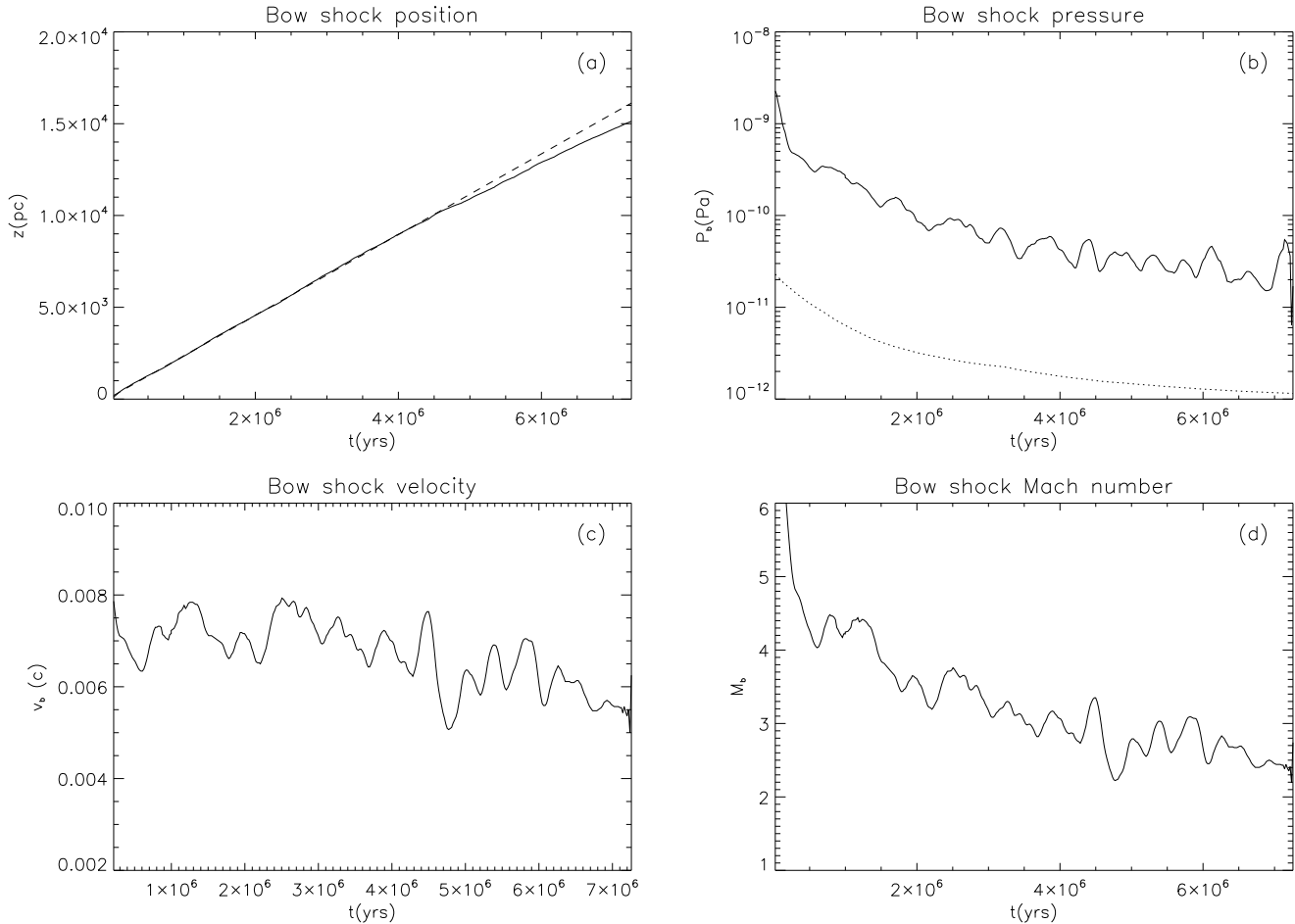


**Figure 3.** Evolution with time of the position (a), pressure (b), instantaneous velocity (c) and Mach number (d) of the bow shock in the axial direction. The bow shock position is selected as the first point of the grid (starting from its end) where the speed is larger than  $10^{-4} c$ . The dashed line in panel a indicates the best fit to the first half of the evolution ( $z \propto 0.0022 t [\text{yrs}] \text{ pc}$ ); deceleration at the last stages is clear. The bow shock pressure is taken as the value in the first maximum, also searched from the end of the grid. The dotted line in panel b shows the pressure of the ambient medium in the region where the bow shock is located at the given time. The instantaneous velocity of the bow shock is computed with the discretized derivative of position with respect to time at each instant, and Mach number of the bow shock propagating in the ambient medium is computed with that advance speed and the mean value of the sound speed in 16 cells ( $2 R_j \equiv 120 \text{ pc}$ ) ahead of the bow shock position. Bow shock pressure, velocity and Mach number curves have been smoothed using an IDL routine (with a 10 point smoothing) in order to avoid the noise coming from the numerical derivative of the bow shock position.

lation are in agreement with the results reported in those papers. We will further discuss this issue in the next Section.

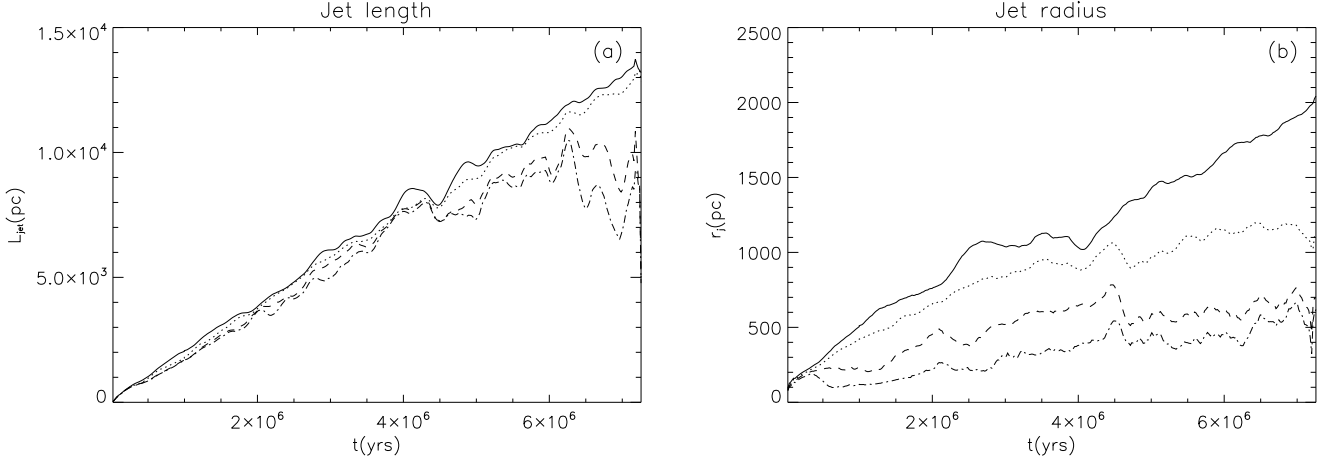
The propagation of the shock leaves behind a region of shocked ambient material through which the jet propagates. In the case of powerful jets, the shock is so strong and its expansion so fast that the region encompassed by the bow shock is almost evacuated with most of the matter concentrated in a thin shell of shocked ambient material behind the shock. The evacuated region is continuously fed by the jet to form an extended cocoon. In the case of weak jets like the one considered here, the bow shocks are correspondingly weaker and the dense region behind the shock, correspondingly wider. Hence the cavity/shell division suitable for the shocked regions surrounding powerful jets transforms into a cocoon/shocked-ambient-medium division. This structure is easily seen in the color maps of rest-mass density and tracer at the end of the simulation, to be discussed in the next section.

Fig. 4 shows the evolution of the jet length (Fig. 4a) and the jet radius (Fig. 4b) with time. Both quantities are calculated for different values of the jet mass fraction. The spreading of the lines in

the jet length plot for  $t > 4.5 \cdot 10^6$  yrs results from the entrainment of ambient material in the head of the jet which causes the deceleration in the jet advance mentioned in the preceding paragraphs. The values of the jet radius for the different mass fractions diverge right from the start of the simulation, implying progressive jet stratification, shearing and mixing, as the jet propagates outwards. The aspect ratio of the jet increases for larger values of the jet mass fraction and is always larger than the aspect ratio of the shocked region.

### 3.1.2 Comparison with Analytical Models

Begelman & Cioffi (1989) developed a simple model for the evolution of the cavities/cocoons surrounding powerful jets in homogeneous ambient media under the assumptions that the jet propagation speed and the power injected into the cavity are independent of time, and that the pressure of the external medium is negligible. The model can still be applied to describe the evolution of the



**Figure 4.** Jet length (a) and jet radius (b) versus time. The different lines stand for the different criteria used to define the jet/ambient transition: solid line is for jet mass fraction  $f = 0.01$ , dotted line for  $f = 0.1$ , dashed line for  $f = 0.5$  and dash-dotted line for  $f = 0.9$ .

shocked regions surrounding weak jets. Then, the mean pressure in the shocked region is given by

$$P_s \propto \frac{L_s}{v_{bs} A_s}, \quad (14)$$

where  $L_s$ ,  $v_{bs}$  and  $A_s$  are the power injected into the shocked region from the jet through the terminal shock, the bow shock speed in the direction of propagation of the jet, and the transversal cross-section of the shocked region (i.e.,  $\pi R_s^2$ ,  $R_s$  being the radius), respectively. The pressure in the shocked region causes it to expand with velocity  $\dot{R}_s$  according to

$$P_s = \rho_a \dot{R}_s^2, \quad (15)$$

where  $\rho_a$  is the ambient density. This implies  $1/R_s \propto \dot{R}_s$ , and hence

$$R_s \propto t^{1/2}, \quad P_s \propto t^{-1}, \quad l_s/R_s \propto t^{1/2} \quad (16)$$

(where in this last expression,  $l_s$  stands for the longitudinal size of the shocked region).

In Scheck et al. (2002), and also in the context of powerful jets, the authors developed a simple extension of Begelman & Cioffi's model to account for the secular deceleration of the jet advance speed due to the expansion of the jet cross-section. According to this model,  $v_{bs} \propto t^\alpha$ , and

$$R_s \propto t^{1/2-\alpha/4}, \quad P_s \propto t^{-1-\alpha/2}, \quad l_s/R_s \propto t^{1/2+5\alpha/4}. \quad (17)$$

In the simulations presented in that paper, a value of  $\alpha \sim -1/3$  was found and, accordingly,

$$R_s \propto t^{7/12}, \quad P_s \propto t^{-5/6}, \quad l_s/R_s \propto t^{1/12}. \quad (18)$$

In the present work, the model is generalized to consider the expansion of the shocked region through an ambient medium with decreasing density. A power law fit of the ambient density (see Fig. 1) with respect to the distance to the source gives  $\rho_a \propto R_s^{-1}$ . With this and taking  $\alpha \sim -0.1$  (from the simulation), we finally have

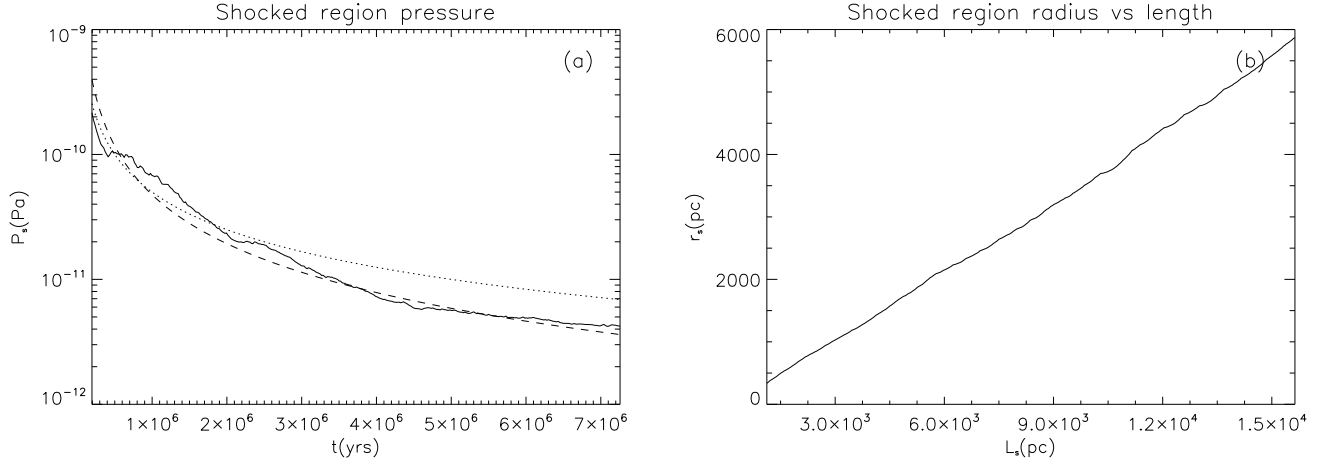
$$R_s \propto t^{0.7}, \quad P_s \propto t^{-1.3}, \quad l_s/R_s \propto t^{0.2}. \quad (19)$$

These results are remarkably consistent with those derived from the simulation ( $R_s \propto t^{0.8}$ ,  $P_s \propto t^{-1.3}$ ,  $l_s/R_s \propto t^{0.2}$ ). Fig. 5a displays the evolution of the pressure in the shocked region versus

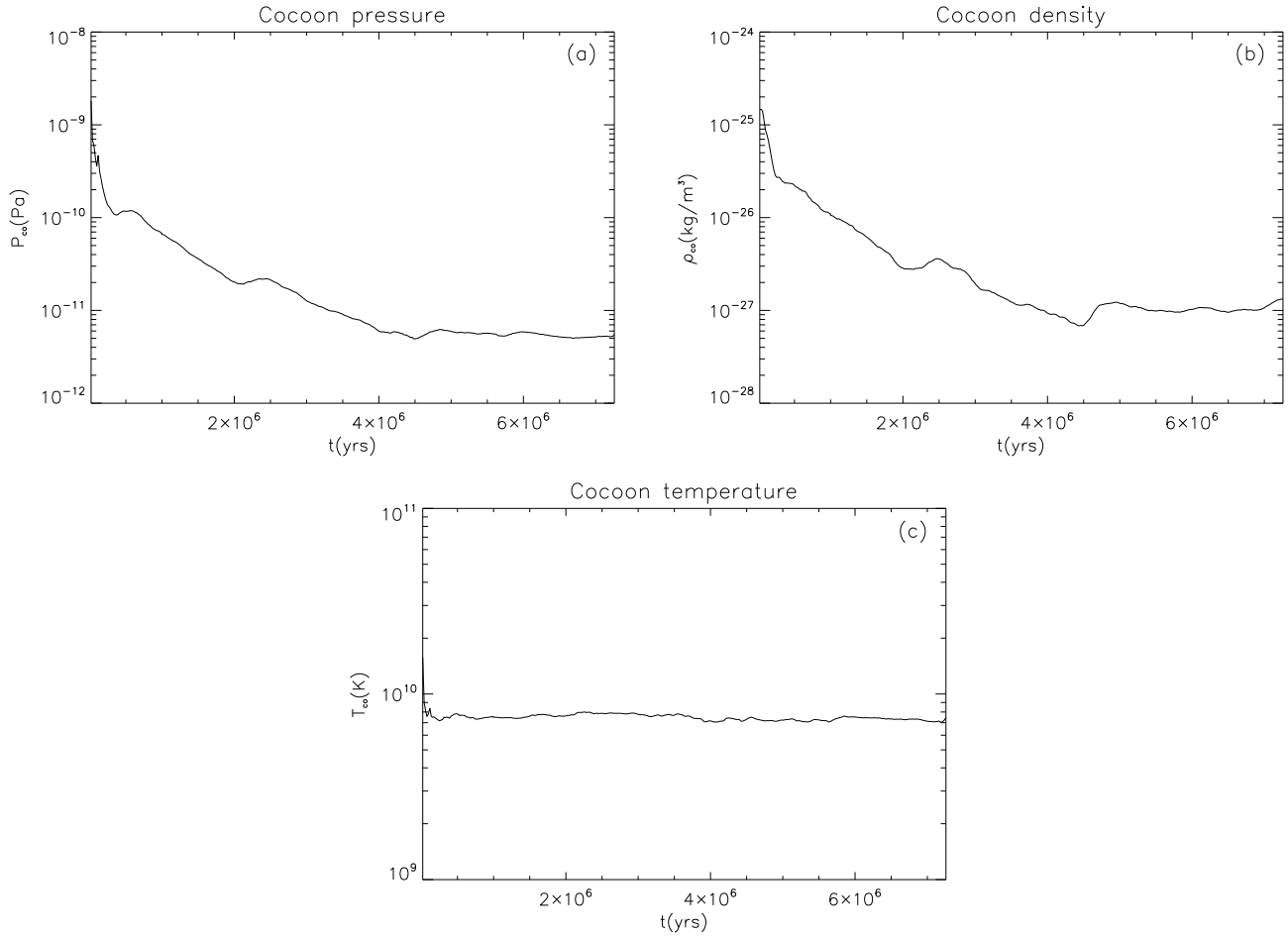
time, together with the  $t^{-1}$  (as in Begelman & Cioffi and Scheck et al. models) and  $t^{-1.3}$  fits. At this point, we must remark that in the simulation we used an open boundary condition in the symmetry plane at the jet basis that allows the leakage of gas and, consequently, a faster pressure drop in the shocked region. A crude *a posteriori* analysis does not allow us to rule out the possibility that the gas internal energy that left the shocked region through the open boundary is of the same order (or  $\sim 1/10$ ) than that remaining in it. However, the agreement between the results from the model discussed above and those derived from the simulation suggests that the flow through the open boundary is effectively negligible. Despite the continuous decrease of the pressure, the shocked region is still overpressured by a factor of 4 with respect to its environment at the end of the simulation. This fact might be alleviated with the introduction of cooling processes. However, Kraft et al. (2003) and Croston et al. (2007) also derived strong overpressure (as much as two orders of magnitude) of the X-ray emitting shells in Cen A and NGC 3801 with respect to the surrounding interstellar media. This is in agreement with our results that give a pressure in the shocked region at  $t \sim 2 \cdot 10^6$  yrs (the approximate age of the jets in Cen A and NGC 3801) more than one order of magnitude larger than that of the ambient medium. Finally, the plot of shocked region radius versus linear size, in Fig. 5b, shows a self-similar growth for the late stages of the simulation (with an aspect ratio for the shocked region of  $\approx 2.7$ ). The deceleration of the jet advance for  $t > 4.5 \cdot 10^6$  yrs, produces a change in the evolution of the aspect ratio of the shocked region that by the end of the simulation has decreased to a value of 2.6.

Fig. 6 show the evolution of the mean pressure (Fig. 6a), density (Fig. 6b) and temperature (Fig. 6c) in the cocoon as a function of time. Remarkably, the cocoon temperature is almost constant in the long term evolution. Also interesting is the fact that the pressure in the cocoon follows a similar evolution to that in the whole shocked region (see Fig. 5a). This last fact can be explained taking into account that the sound speed in the cocoon/shocked-ambient-medium region, is about one or two orders of magnitude larger than its expansion velocity, hence allowing for an almost instantaneous (with respect to the dynamical time scale) adjustment of the pressure. An example of this is seen in the pressure map at the end of the simulation to be discussed in the next section.

The isothermal evolution of the cocoon can be explained by



**Figure 5.** The panels show the pressure in the shocked region versus time (a) and the radius of the shocked region versus its length (b). The pressure is computed as the mean pressure in all the cells with shocked ambient medium. The dotted line shows the evolution as  $\propto t^{-1}$  and the dashed line gives the best fit of the curve  $t^{-1.3}$ . The radius is calculated as the mean radius of the bow shock, with this position determined by a lateral motion larger than  $10^{-4}$  c, see caption of Fig. 3. The length of the shocked region used in this plot as the abscissa coincides with the bow shock position shown in the panel a of Fig. 3.



**Figure 6.** Mean pressure (a), density (b) and temperature in the cocoon as a function of time (c). The cocoon is defined as the region with tracer values between 0.01 and 0.3.



assuming that the almost self-similar evolution of the shocked region extends also to its internal structure. As discussed in the previous paragraph, for the pressure in the cocoon,  $P_c$ , we have, at any time,

$$P_c \sim P_s \propto \frac{L_s}{v_{bs} A_s}. \quad (20)$$

The density in the cocoon,  $\rho_c$ , can be estimated, in a similar way, as the quotient of total mass injected in the cocoon,  $J_c t$ , and its volume. If  $A_c$  is the transversal cross-section of the cocoon, then

$$\rho_c = \frac{J_c}{v_{bs} A_c}. \quad (21)$$

On the other hand, for the temperature in the cocoon,  $T_c$ , we have  $T_c \propto P_c / \rho_c$ , and, from the two previous equations,

$$T_c \propto \frac{L_s}{J_c} \frac{A_c}{A_s}. \quad (22)$$

Now, the independency of  $T_c$  follows if the fluxes of energy and mass through the jet terminal shock are constant and the evolution of  $A_c$  and  $A_s$  with time is the same.

### 3.2 Fate

Figs. 7-9 show several maps of different quantities at the end of the simulation ( $t = 7.26 \cdot 10^6$  yrs). The morphological features observed in the panels are those of a typical jet (see, e.g., Martí et al. 1997): a bow-shock propagating through the unperturbed ambient gas (clearly seen in the top panel of Fig. 7 displaying the logarithm of the rest-mass density), a cocoon composed of mixed jet and ambient matter, and the jet itself propagating inside. The cocoon, formed by mixed jet material, is better observed in the bottom panel of Fig. 7 displaying the jet mass fraction. Both maps show how the jet initially expands up to a distance  $z \sim 1.5$  kpc from the source<sup>2</sup> and then recollimates and oscillates until it is disrupted, i.e., until the ambient medium material reaches the jet axis (at  $z \sim 4.5$  kpc), due to entrainment of the external medium. Fig. 8 shows the flow Lorentz factor (top panel) and the axial velocity (bottom panel). A relativistic jet (with maximum Lorentz factor of 5.3) is seen up to the disruption point at  $z \sim 4.5$  kpc. After this point, strong deceleration of the flow associated with mass loading of the jet is observed in both maps. The axial velocity plot reveals a mildly relativistic backflow in the cocoon. However, these high speeds can be an artifact of the imposed axisymmetry, as discussed in Aloy et al. (1999) on the basis of 3D simulations of relativistic jets. The use of open boundaries on the symmetry plane at the jet base could also maintain artificially large pressure gradients along the cocoon leading to high speed backflows (see the discussion in sect. 3.1.2). Fig. 9 shows maps of the logarithm of temperature (top panel) and pressure (bottom panel). The bow shock, cocoon and jet structure are also clearly seen in these maps. As can be seen in the top panel of Fig. 9, the ambient temperature increases by a factor of a few behind the bow shock and by two orders of magnitude in the cocoon due to the mixing with hot plasma injected through the terminal shock at the head of the jet. Also in this panel, Kelvin-Helmholtz instabilities arising in the interface between the outer subsonic backflow in the cocoon and the shocked ambient medium are observed. Finally, the bottom panel of Fig. 9 shows a shocked

region with an homogeneous pressure distribution and a series of waves emanating from the outer part of the cocoon.

The profiles of several variables along the jet axis (rest-mass density, pressure, jet mass fraction, Lorentz factor, axial velocity and temperature) at the end of the simulation are plotted in Fig. 10. Fig. 11 shows averaged values of rest-mass density, pressure, Mach number and flow Lorentz factor along the jet at the same time. From these plots and the maps in Figs. 7-9 we can obtain a general picture of the evolution of the jet in terms of its dynamics. Close to the injection point, the flow can be considered as steady. The jet initially expands in the ambient density gradient. The expansion accelerates (Fig. 8), rarefies (Fig. 7) and cools (Fig. 9) the flow. This is seen in more detail in the cuts along the jet axis shown in Fig. 10. After a short distance, in which the variables remain constant, a strong adiabatic expansion produces a fast decrease in density, pressure and temperature on the jet axis, up to  $z = 1.5 - 2.0$  kpc. At the same time, there is a strong acceleration seen in the plots of Lorentz factor and axial velocity. The jet overpressures again in a standing shock at  $z \sim 2$  kpc from the source. The shock is seen in the maps and plots of density, pressure and temperature as a sudden increase and, in those of velocity and Lorentz factor, as a strong deceleration of the flow. The overpressure of the jet with respect to the ambient (see the pressure map in Fig. 9, and the plots in the Figs. 10b and 11b) results in a new phase of expansion. Each expansion is followed by a recollimation shock that produces significant deceleration of the jet (see Fig. 8 and Figs. 10d and 10e). Up to three recollimation shocks (at  $z \sim 2$  kpc,  $z \sim 3$  kpc and  $z \sim 4.5$  kpc) are observed before the jet is disrupted. These shocks can be clearly identified in the Lorentz factor and velocity plots in Fig. 10 (panels d and e). The planar/conical shape of these shocks could be an artefact of axisymmetry, but at the distances from the central source at which these shocks are formed (i.e. a few kpc), 3D effects are probably small. After the first shock, the jet is less overpressured with respect to the ambient medium and it expands in an atmosphere with a smoother density gradient. This makes the next standing shocks milder (see the pressure plots in Fig. 10b and Fig. 11b). At  $z > 6$  kpc (i.e., behind the terminal shock), the jet is overpressured with respect to the ambient (Fig. 11b) due to the heating of the flow in shocks, as seen in Fig. 10f.

The Lorentz factor is between 2 and 5.3 in the whole section of the jet up to the first recollimation shock, at  $z \sim 2$  kpc (see Fig. 8). After this shock, the flow is relativistic in filaments far from the axis, as the portions of the jet closer to the axis are decelerated by the shock. The averaged Lorentz factor (Fig. 11d) decreases from 4.3, after the first adiabatic expansion of the jet, to a value of 1.15 at the disruption point, which we define as the point in which ambient material reaches the axis (see the jet mass fraction map in Fig. 7, the flow Lorentz factor map in Fig. 8, and the corresponding axial cuts in Figs. 10c and 10d). The internal Mach number of the flow (Fig. 11c) also decreases along the jet up to the terminal shock where the flow becomes subsonic. After the terminal shock, the flow is only slightly relativistic, with velocities around  $0.5 c$ . It is also remarkable that in the cocoon a backflow with mildly relativistic speeds is established right down to the central regions of the parent galaxy.

The jet remains well collimated and relativistic up to the disruption point. However, after this point, the subsonic character of the flow triggers the process of mixing with the ambient medium, as already pointed out by Bicknell (1995). The rest-mass density plots (Figs. 10a and 11a) show the increase of this variable as the jet entrains ambient material for  $z > 4.5$  kpc. The position of the disruption point oscillates throughout the simulation from

<sup>2</sup> Throughout this section and in the discussion of results,  $z$  will refer to distances to the galactic source, located 500 pc away from the injection in the grid.

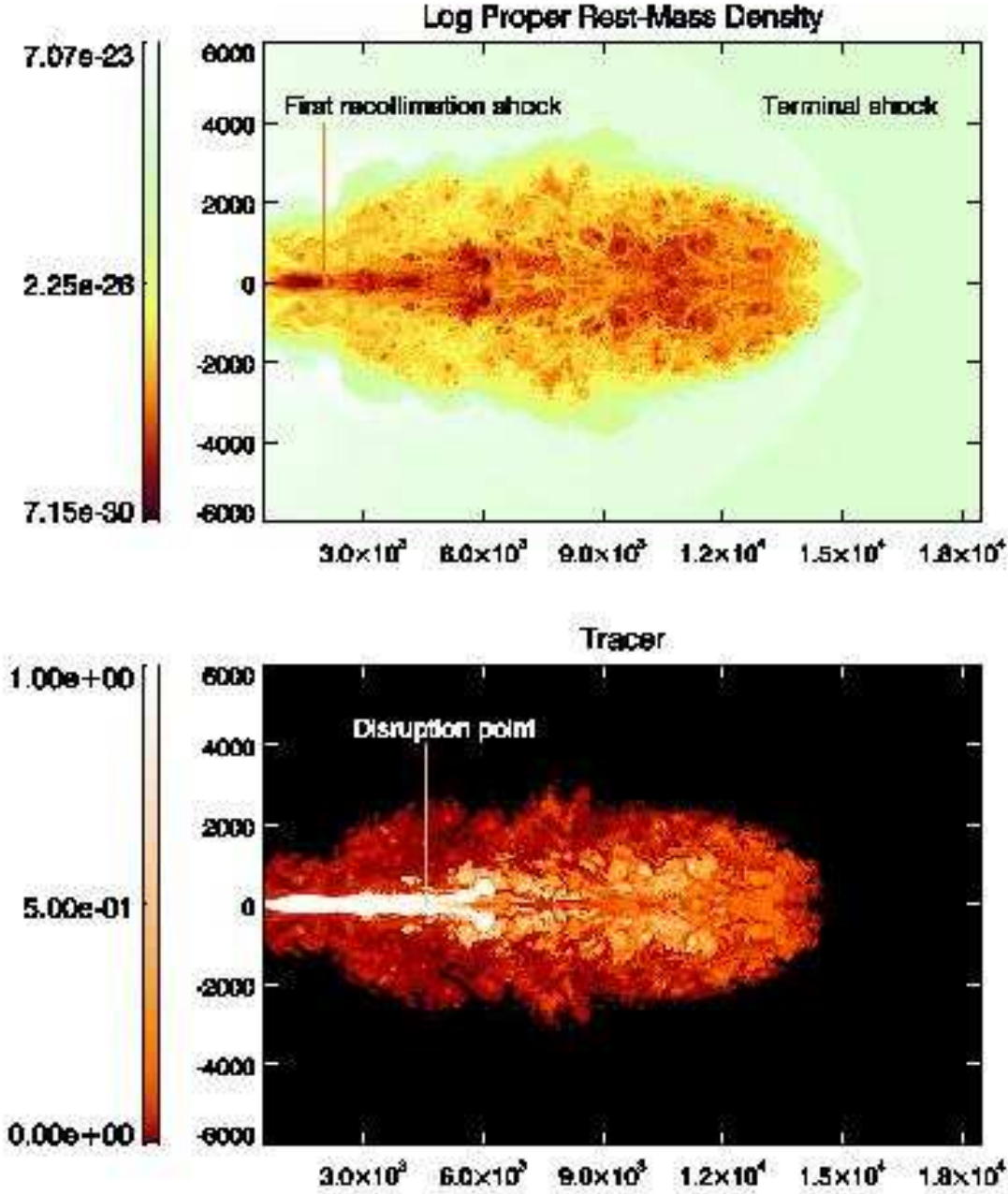


**Figure 7.** Logarithm of rest mass density (top panel) in  $\text{kg/m}^3$  and jet mass fraction (used as a tracer for the jet plasma; bottom panel) at the last frame of the simulation in this work. The locations of the first recollimation shock and the terminal (or bow) shock are indicated in the rest mass density map, and the disruption point is indicated in the jet mass fraction map. Coordinates are in parsecs.

$z \sim 2.5 - 3.5$  kpc to  $z \sim 6 - 7$  kpc. This non-monotonic advance is due to the complex dynamics of the terminal shock, which changes periodically from planar to conical, as already noted in previous long-term simulations of jets (see, e.g., Martí et al. 1997; Scheck et al. 2002). In the phases in which the disruption point moves backwards, the further injected plasma accumulates in the region between injection and disruption, thus increasing the pressure in the jet, that ultimately *bursts*, expanding the unmixed jet outwards and bringing the disruption point farther from injection.

Fig. 9 shows that the temperature in the cocoon is of the same order, but larger than that of the jet ( $T \sim 10^9 - 10^{10}$  K,

cf  $T_j = 4.1 \cdot 10^9$  K at injection). In addition, the gas in this high temperature region can be up to an order of magnitude denser than the jet (top panel in Fig. 7) due to the loading with baryons from the ambient (jet mass fraction,  $f < 0.2$ ). However, despite this large baryon load, the number of leptons is still between 20 and 200 times larger than the number of baryons in this region. Leptons are heated in shocks inside the jet (see top panel of Fig. 9) and at the terminal shock. The high temperatures achieved in the cocoon are a consequence of the small amount of baryons. The adiabatic exponent in the cocoon remains close to the relativistic limit of  $4/3$ .

In a recent paper, Kino, Kawakatu and Ito (2007) conclude

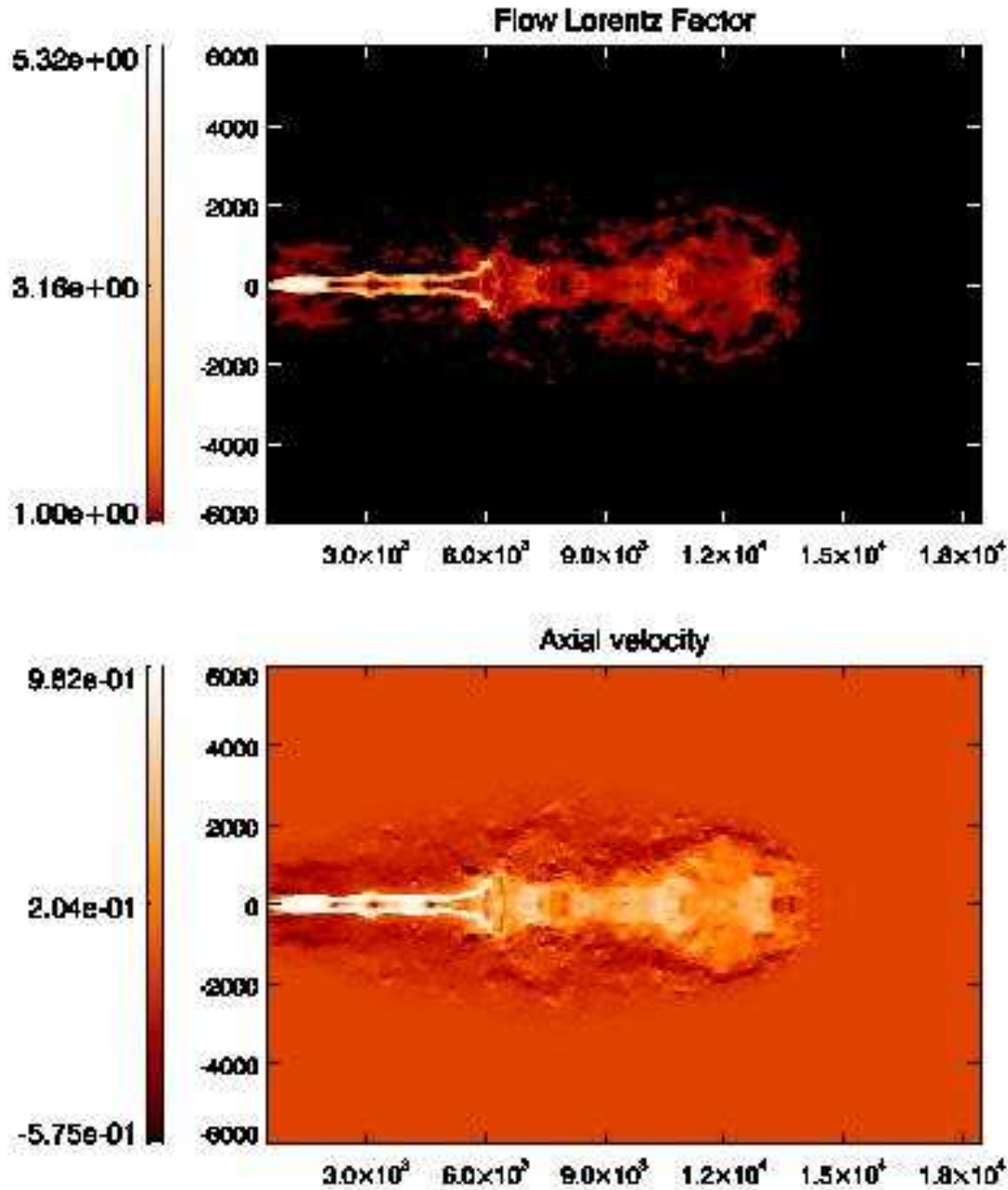


**Figure 8.** Lorentz factor (top panel) and axial velocity (bottom panel) in units of  $c$  at the last frame of the simulation in this work. Coordinates are in parsecs.

that the temperature of the cocoon gas for an FRII jet with Lorentz factor 10 could be of about  $1.2 \cdot 10^{10}$  K, a value close to that obtained in our simulation. In the case of FRII jets, the particles are heated in the hot spot, the heating depending on the strength of the shock. In a electron-positron FRI jet like that simulated here, the particles are heated in the strong recollimation shocks along the jet. This effect can compensate the lack of heating at the terminal point of the FRI jet due to its low power. Thus, the temperature in the cocoon remains high as long as the pollution by baryons is low.

### 3.3 Additional simulations

The modelling of 3C 31 presented in LB02b divides the inner 12 kpc of the jet into three regions: inner, flaring and outer region. The authors suggest that the boundary between the inner and flaring regions (at 1.1 kpc from the source) consists of a discontinuity in velocity, density and pressure, which is the cause of the sudden increase of radio emission. In Canvin & Laing (2004), Canvin et al. (2005) and Laing et al. (2006), the inner and flaring regions of the sources studied are defined in terms of emissivity, but the authors do not invoke the presence of a shock in the transition from one region to the next. In this paper we identify that transition as due to the presence of a recollimation shock. Within this frame, we com-

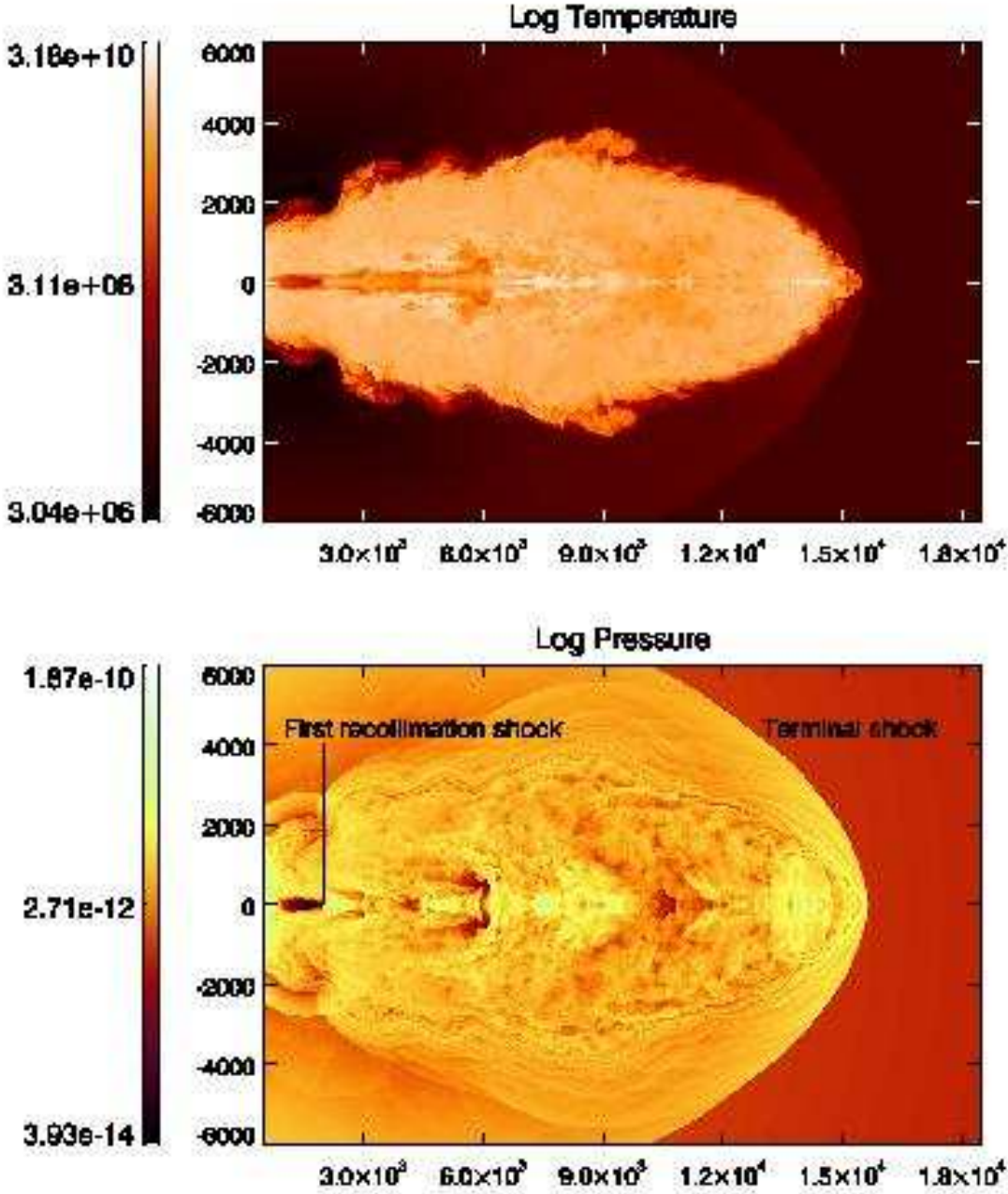


**Figure 9.** Logarithm of temperature (top panel) in K and logarithm of pressure (bottom panel) in Pa at the last frame of the simulation in this work. The position of the first recollimation shock and the terminal (or bow) shock are indicated in the pressure map. Coordinates are in parsecs.

pare the properties of the observed discontinuity with those of its counterpart in the numerical simulation at  $z \sim 2$  kpc.

LB02b give a speed of the jet of  $0.87 c$  in the inner region, that we used as the injection speed of the jet in our simulation. However, the flow in the simulation expands adiabatically and accelerates in the decreasing density ambient medium, entering the first recollimation shock with a larger speed ( $\sim 0.98 c$ ). The technique used in LB02a that allows for a fitting of the velocity of the jet is not adequately constrained in the inner region, so the initial velocity used here may be in error. The authors report that jet/counter-jet ratio is slightly smaller in the inner region than at the start of the flaring region, which could be interpreted as due to an acceleration of

the flow in this region, as observed in our simulation. Observations with higher transverse resolution and sensitivity could potentially constrain any acceleration in the inner region.

The position and velocity of the flow upstream/downstream of the standing shock depend on the acceleration of the jet in the initial adiabatic expansion phase. Similarly, the properties of the flow upstream the shock determine the properties downstream the shock and ultimately the jet disruption. In order to study the influence of jet pressure and injection velocity on the evolution of the jet, we performed three additional simulations with the following properties: a) Simulation 2,  $v_j = 0.5 c$ ,  $P_j/P_{a,c} = 3.8$ ; b) Simulation 3,  $v_j = 0.6 c$ ,  $P_j/P_{a,c} = 7.8$ , and c) Simulation 4,  $v_j = 0.5 c$ ,

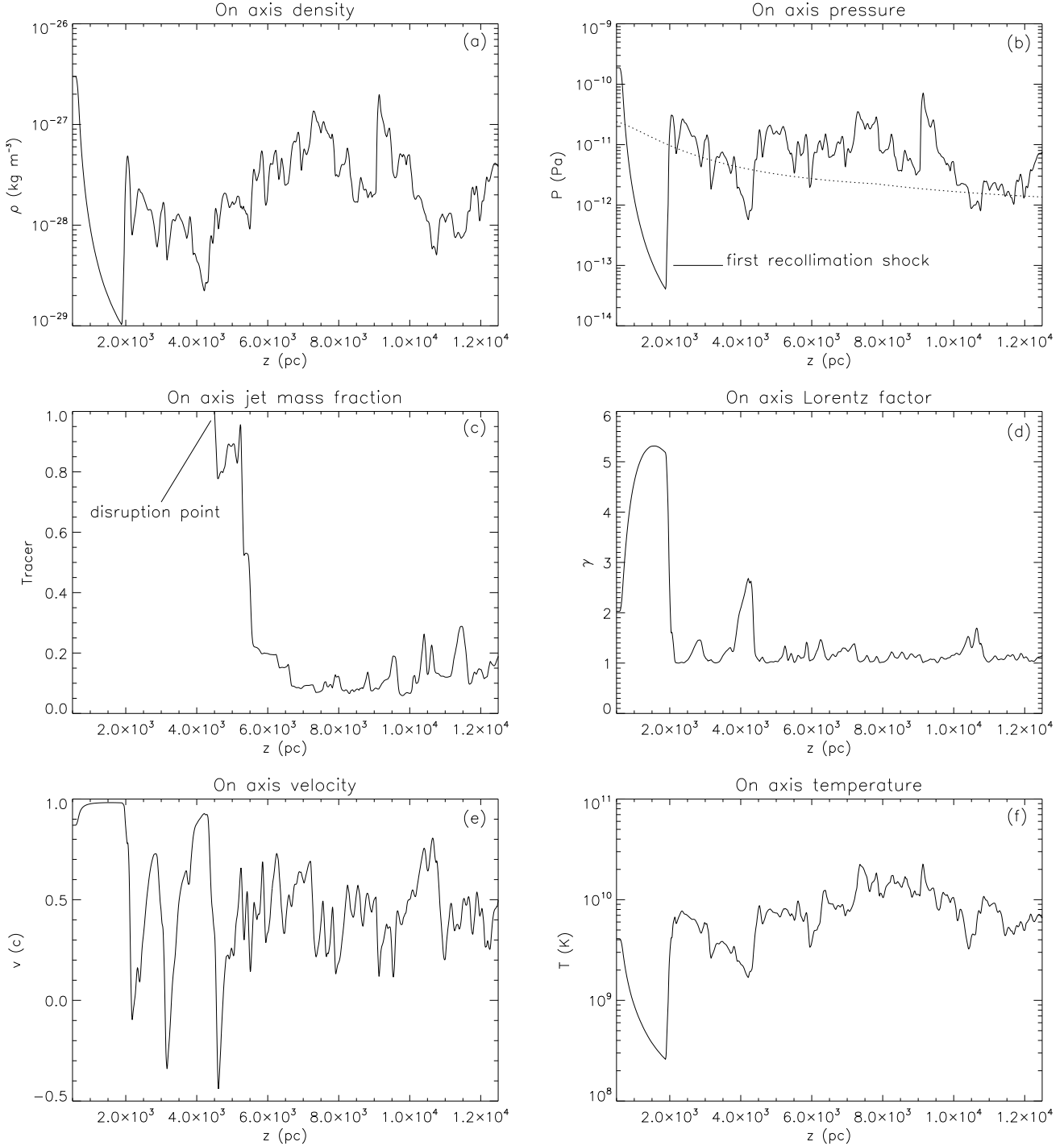


**Figure 10.** Different profiles of variables on the jet axis at the end of the simulation. The different panels show the rest mass density (a), pressure (solid line) and original ambient medium pressure on the axis (dotted line; b), jet mass fraction (c), flow Lorentz factor (d), axial flow velocity (e) and temperature (f). The location of the first recollimation shock is indicated in the pressure plot (panel b) and the location of the disruption point is indicated in the jet mass fraction plot (panel c).

$P_j/P_{a,c} = 1$ . The change in the flow injection velocity and the jet pressure in these additional simulations produces a change in the power of the jet. In the case of simulation 2, the change in the injection parameters produces a reduction of the jet power of about an order of magnitude with respect to the original simulation. In the case of simulations 3 and 4, the reduction in power with respect to

the first simulation is of a factor of 3 and 30, respectively. Finally, in these simulations we have used approximations to the Bessel functions that are solved in the equation of state -see the Appendix-(de Berredo-Peixoto et al. 2005; Service 1986), in order to reduce the computational load.

In simulation 2, the jet flow is accelerated in the pressure gra-

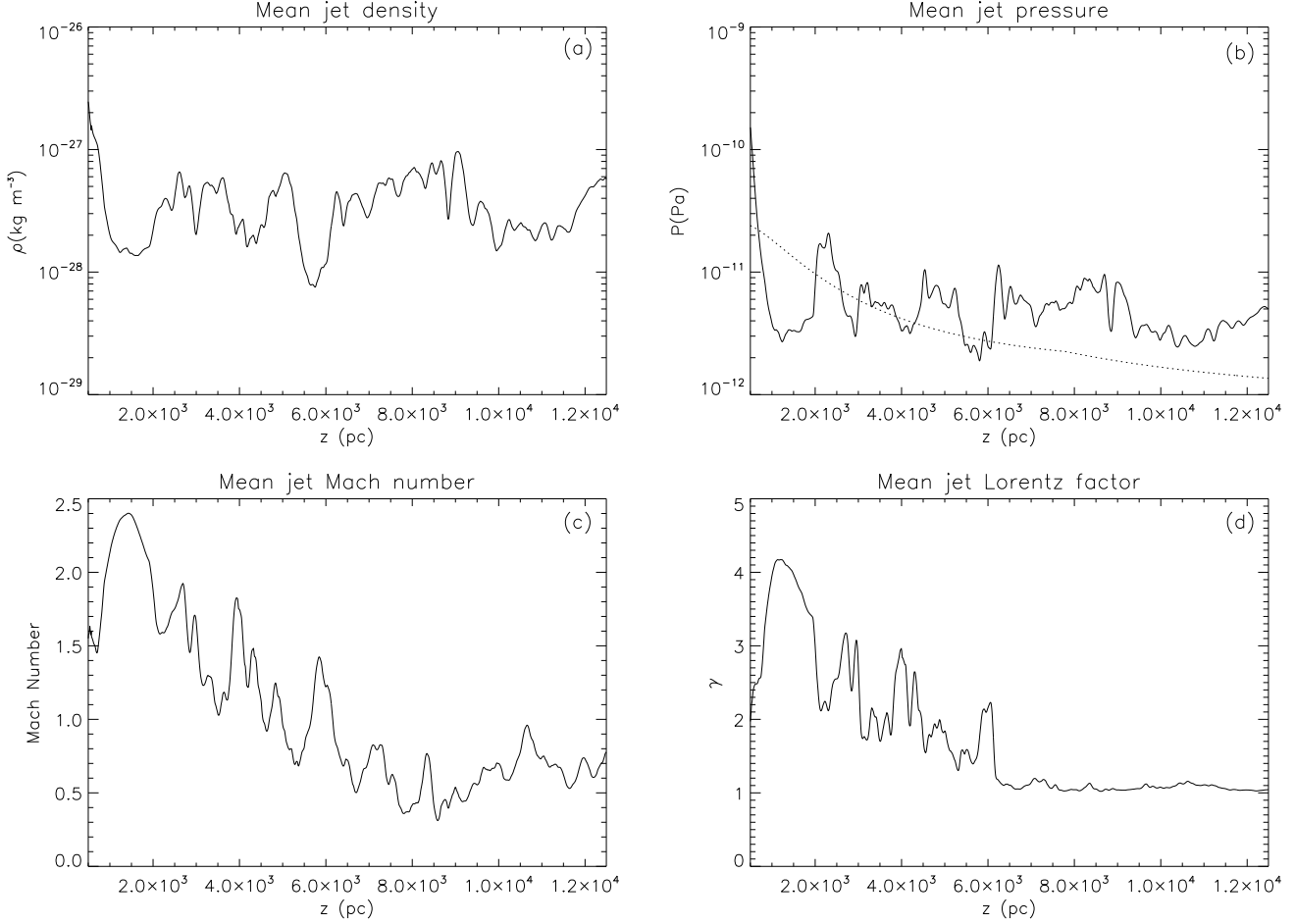


**Figure 11.** Profiles of radially averaged variables, weighted with the tracer and counting only those cells where the axial velocity is significantly larger than zero ( $v^z > 10^{-3} c$ ). The different panels show the rest mass density (a), pressure (solid line) and original ambient medium pressure on the axis (dotted line; b), Mach number (c), and Lorentz factor (d).

dient up to  $v_j \sim 0.82 c$ . The first recollimation shock occurs at  $z \sim 700$  pc, closer to the source than given by LB02b, due to the smaller initial pressure ratio at injection and the smaller injection speed. After this shock, the jet is strongly mass loaded and decelerated to speeds  $v_j < 0.5 c$ . The entrained jet expands and accelerates slightly to  $v_j = 0.6 c$ , but the latter expansion ends up in further mass loading and deceleration of the jet at  $z \sim 1.1$  kpc. Mass loading and deceleration continue downstream up to  $z = 4.8$  kpc, where the velocity of the jet is already subrelativistic and subsonic. The simulation was stopped when the head of the jet had reached this distance, at time  $t \sim 6.6 \cdot 10^6$  yrs.

The jet in simulation 3 goes through the first recollimation shock at  $z \sim 800$  pc. The flow enters the shock with a speed  $v_j \sim 0.94 c$ . After the shock, the jet decelerates and is disrupted at  $z \sim 1.5$  kpc. As in simulation 2, mass loading continues downstream. The simulation was stopped at  $t \sim 6 \cdot 10^6$  yrs, when the jet head is at  $z \sim 5$  kpc and the bow shock is at  $z \sim 6$  kpc.

Simulation 4 differs from simulation 2 in that the jet is in pressure equilibrium with the ambient medium at injection. This difference prevents the formation of strong shocks. The jet velocity oscillates close to the injection value ( $v_j = 0.5 c$ ). Successive expansions and contractions, i.e. smooth recollimations, in the pressure gradient cause the pinching of the jet. The growth in amplitude of this pinching as it couples to a Kelvin-Helmholtz instability mode

causes entrainment and the disruption of the jet. The jet is more stable in this case simply because the amplitude of the recollimation shocks is reduced. Nevertheless, the jet is light and slow, which makes it a good candidate for disruption due to the growth of instabilities (Perucho et al. 2004, 2005). At the end of the simulation ( $t \sim 7 \cdot 10^6$  yrs) the jet head is at  $z \sim 4.8$  kpc.

#### 4 DISCUSSION

Scheck et al. (2002) performed a series of simulations of the long term evolution of jets with different compositions evolving in a uniform density ambient medium. The initial power of those jets was typical for FR II sources. Compared to their simulations, the jet in the simulation presented here is 100 times weaker. The bow shock propagates at a slightly larger mean velocity in our simulation. This fact is due to the simulated jet being overpressured and propagating through a decreasing density atmosphere. The morphology of our jet is close to that of model LH (leptonic, hot) in Scheck et al. (2002), although in our case, the jet is more pinched and presents entrainment behind the head. It is remarkable that the jet in our simulation is leptonic and hot and the structure obtained is solely similar to the same case in Scheck et al. (2002).



#### 4.1 Jet advance speed and source age

Parma et al. (2002) studied a sample of FRI radio galaxies and estimated their spectral ages from two-frequency data. Although these measurements are subject to uncertainties, as pointed out by Laing et al. (2006) and Katz-Stone & Rudnick (1997), mainly due to possible confusion between jet and lobe emission, we have used them in order to make a rough comparison of the age of the source in the simulation with those of FRIs. The ages obtained by Parma et al. (2002), claimed to be lower limits, range between  $10^7$  and  $10^8$  yrs, in general larger than those of FRII jets. From these estimates, the authors compute advance velocities for the lobes in the range  $10^{-3} - 10^{-2} c$ . VLA observations of 3C 31 (e.g., LB02a) show jet material at projected distances up to 150 kpc. Considering a viewing angle of  $52^\circ$  (LB02a), this implies linear distances of about 200 kpc. From the advance velocities found in the simulation, we can put constraints on the time that the source has been continuously active. The continuity is supported by the fact that there are no emission gaps in the images. At the typical advance speeds found in this simulation, say  $5 \cdot 10^{-3} c$  for further advance of the head as an upper limit, the age of the source would be  $t > 10^8$  yrs, in agreement with the spectral ages given by Parma et al. (2002). The lower limit takes into account further deceleration of the head, and the curved trajectory of the plasma observed in the source at distances larger than  $\sim 25$  kpc. Moreover, low-resolution images show emission out to 300 kpc. The uncertainty in the viewing angle at large distances from the core makes difficult the use of this value for an estimate. Nevertheless, this fact makes of the value given here a strict lower limit. In the frame of intermittency models for the activity in AGNs, the lower limit of the age of the source given here puts constraints on the possible intermittency of 3C 31: either the periodicity is as long as 0.01 – 0.1 times the age of the Universe, or it has been continuously active since the onset of its activity.

#### 4.2 Early evolution and the young counterparts of FRIs

We have shown, in Fig. 2, that the evolution of the source in the compact phase is divided in two stages: the *CSO-like* and the *weak CSS-like* phase. Drake et al. (2004) have proposed that low-power CSS sources can be the young counterparts of large FRI sources. Based on spectral aging, the authors give age estimates of  $\sim 10^5$  yrs for several of these CSS sources with linear sizes of a few kiloparsecs, and derive expansion velocities of  $0.004 - 0.007 c$ . These velocities are in agreement with those derived from the simulation (see Fig. 3). Furthermore, the age of the simulated jet in the *weak CSS-like* phase ( $t \sim 10^5 - 10^6$  yrs) is of the order of that estimated by Drake et al. (2004) for the observed low-power CSS sources, and its morphology is irregular, as those authors show to be the case of the low-power CSS jets. Fig. 2 tells us that FRIs could first go through a CSO stage, characterized by a regular, expanding jet, and, after developing a strong shock due to underpressuring with respect to the ambient medium, at a distance of the order of 1 kpc (depending on the properties of the host galaxy and the jet, as we have seen in Sect. 3.3), develop the irregular structure observed in the maps for the low power CSS sources. Therefore, powerful CSO sources could be the young FRII sources, but, from our results, we predict that low power CSOs could be the young FRI sources.

#### 4.3 Cocoon temperature and emission

The high temperature of the fluid in the cocoon (Figs. 7-9) deserves some discussion. Heating of the jet plasma occurs at the standing shocks along the jet, as shown in Fig. 10f. The efficiency of the heating depends on the strength of these shocks, which ultimately depends on the jet power. In the case of the mildly relativistic, hot jets like those considered in the present work, this last quantity is dominated by the internal energy density flux (or pressure). This is why simulations 2 and 4, with values of initial pressure ratio ( $P_j/P_{c,a}$ ) of 3.8 and 1, respectively, display weaker recollimation shocks and the temperature of jet material hardly rises above the injection values. In any case, the temperatures found in the cocoon ( $T \sim 10^{10}$  K), in combination with the resulting cocoon densities ( $n_{e+,e-} \sim 10^{-3} \text{ cm}^{-3}$ ), would produce a flux at 1 MeV of  $\nu F_\nu \sim 10^{-19} \text{ erg cm}^{-2} \text{ s}^{-1}$  for a source located at the distance of 3C 31, quite below the detection limits of *INTEGRAL* and *NeXT* (Kino et al. 2007, and references therein), and the resulting spectrum would also fall below the detection limits of the X-ray satellite *XMM-Newton*. Moreover, Kino et al. (2007) conclude that the bremsstrahlung luminosity decreases with time as  $t^{-1}$ , from the results of a cocoon expansion that follows basically the same time dependence as that found in this simulation. Thus, the present bremsstrahlung luminosity should be 10 times smaller than that computed here, on the basis of the calculated age of the source compared to the simulated time. In this respect, Kino et al. (2007) show that bremsstrahlung cooling of the cocoon is only important in the very first stages of the evolution ( $t < 200$  yrs). This validates the adiabatic treatment of the problem. We want to point out that the bremsstrahlung emission calculated for the shocked ambient medium is even smaller. Zanni et al. (2003) performed a series of simulations of supersonic and underdense jets in a decreasing pressure atmosphere and showed that jets evolve in two different phases regarding their high energy emission: a phase in which the shell formed by shocked material is highly overpressured and radiative, and a later phase in which the shock is weaker and a deficit of X-ray emission is expected from the lobes. The jet in our simulation is in the former of the two phases. However, Zanni et al. (2003) point out that jets with low density ratios, as that simulated here, form wide and not very dense shells from which no strong emission is expected, in agreement with the results given above. Finally, the recent discovery of bow shocks in low power radio jets (Kraft et al. 2003; Croston et al. 2007), moving at similar Mach numbers as those obtained here, and showing overpressure by more than an order of magnitude with respect to the ambient medium, gives support to our results regarding the dynamics of the bow shock (see next subsection).

#### 4.4 Bow shock

At the end of the simulation, the head of the bow-shock has reached a distance of  $\sim 15$  kpc from the injection position. It expands self-similarly and at basically constant rate ( $\sim 7 \cdot 10^{-3} c$  in the axial direction), with a slight deceleration with time. The bow shock is still supersonic by the end of the simulation ( $M \sim 2.5$ ), contrary to what is expected for an FRI jet in theoretical models, which predict trans-sonic speeds for shocks at such distances. However, recent X-ray observations by Kraft et al. (2003) and Croston et al. (2007) show the presence of bow shocks with Mach numbers between 3 and 8 in the low power radiogalaxies Centaurus A and NGC 3801 at distances of a few kiloparsecs from the source. Taking into account that the jets in 3C 31 are among the most powerful ( $10^{44} \text{ erg/s}$ ) in

FRI sources, it is plausible that the bow shock is long lived in this source. Furthermore, as we have shown in the previous paragraph, we have only simulated less than 10% of the real evolutionary time of the source. Thus, it is possible that, after the simulated time, the bow shocks may naturally decelerate to trans-sonic velocities. The properties and morphology of the jet would then be modified, accommodating the further evolution of the flow to the observed structure of 3C 31, where no bow-shock is observed, and the emission appears to fade gradually with distance.

Table 3 shows the values of number density, temperature and pressure at both sides of the bow shock in our simulation, compared to those given in Kraft et al. (2003) and Croston et al. (2007) for Cen A and NGC 3801, respectively. The jump in density at the head of the bow shock, in the axial direction, has a value of 3.7, close to the Rankine-Hugoniot jump condition limit for strong shocks, similar to the case of NGC 3801. The jump in pressure in the simulation is smaller than in the observations of Centaurus A and NGC 3801, which can be understood in terms of the age of the jets: the jet in the simulation is older than those in Centaurus A and NGC 3801 and therefore the bow shock is slightly closer to equilibrium with the external medium. The main differences between the simulation and the observations arise in the temperature. In a direction transverse to the jet axis, the temperature of the shocked ambient medium is of the order of that in Centaurus A. However, in the head of the bow shock, the temperatures of the shocked gas reach values of  $10^9$  K, too high compared with observations. This difference may be due to 3C 31 being more powerful than the observed sources and also due to the lack of cooling mechanisms in the simulation. Apart from this, the results obtained from the simulation are in fair agreement with the X-ray observations of the aforementioned sources. Therefore, we conclude that 3C 31 possibly went through a similar stage to that observed for Centaurus A and NGC 3801, and only in later stages than those simulated here, the bow shock decelerated to transonic speeds and disappeared.

#### 4.5 Jet structure and the Laing & Bridle (2002a,b) model

The final structure of the jet is analyzed in the following paragraphs. We observe a fast adiabatic expansion when the jet leaves the galactic core, as the jet propagates through the steep density gradient of the galaxy. This expansion ends at  $z \sim 2$  kpc and it is followed by a sudden recollimation. This recollimation generates a new overpressuring of the jet, and thus, a second expansion. The smoother pressure and density gradient of the atmosphere in the region where the second expansion takes place, causes it to appear smoother than the first expansion. This process ends, as in the previous case, in a recollimation shock, at  $z \sim 3$  kpc. The third standing shock is at  $z \sim 4.5$  kpc, after which the jet, strongly entraining and decelerated by mass loading, generates a wide shear layer.

The structure of the jet at the end of our simulation is to be compared with that given in the dynamical model for the jet of 3C 31 in LB02b. The main caveat for comparison between the simulation and the observations and modelling in the latter paper is that the jet in our simulation has not reached a steady-state, but keeps evolving. This is clearly observed in the overall structure of the jet seen in Figs. 7-9 compared to the images of the jets in 3C 31. The main difference is the presence of lobes in the simulation: these are not observed. Laing et al. (2006) have shown that the kinematics of the jets in 3C296 (which are surrounded by their lobes) may be affected by the absence of a shear layer with the ambient medium.

In LB02b, the inner 12 kpc of the jet are divided into three

regions: inner, flaring and outer. The inner region (up to 1.1 kpc) consists of a fast moving flow  $v \sim 0.8 - 0.9 c$  that enters the flaring region (1.1 – 3.5 kpc) through a discontinuity that decelerates the flow and increases the emissivity. In this region, the authors observe a spread of the isophotes and a subsequent recollimation. The outer region (3.5 – 12 kpc) is characterized by a slow decrease in velocity, and continuous mass-loading. In our simulation, the discontinuity between the inner and flaring region is identified with the recollimation shock at  $z \sim 2$  kpc. LB02a argue that the velocity of the jet is about  $0.8 c$  up to about 3 kpc. In our case, however, after the standing shock, the velocity already drops to about  $0.4 c$ . Moreover, LB02b found that the entrainment rate required to counterbalance the effects of adiabatic expansion and keep the velocity fairly constant at the beginning of the flaring region was consistent with that expected from mass injection by stellar winds. This points towards a fundamental difference between our simulation and their modelling, mainly due to the lack of mass load from stellar winds and the presence of a standing shock in our case. However, such a shock could explain discontinuities in emissivity found close to the start of the flaring regions in the observations and modelling of the sources studied by LB02a,b, Canvin & Laing (2004), Canvin et al. (2005) and Laing et al. (2006), and the observation of high energy emission from the flaring regions in 3C 31 (Hardcastle et al. 2002), NGC 315 (Worrall et al. 2007) and 3C 296 (Hardcastle et al. 2005; Laing et al. 2006). On the other hand, strong recollimation is not evident from the shapes of the jets in the sources studied, although it could be occurring in the inner parts of the jet, whereas the outer layers show constant or increasing radius, as shown by our simulation, where the radius of the outer layers shows little signs of recollimation, contrary to the case of the core of the jet (Fig. 4b and Figs. 7-9).

In the simulation, the transition between the flaring and outer regions occurs at  $z \sim 4$  kpc, after the third recollimation shock, and not as a slight underpressuring and recollimation of the jet that generates a smooth continuation between both regions, as required by the model of LB02b. Although there is no observational evidence for recollimation shocks in this region, these outer shocks in the simulation are milder than the first, so no strong emission from such structures would be expected. The oscillations of the jet pressure around pressure equilibrium captured by the simulation in the outer region are still strong enough to generate shocks, though milder than the previous ones. This difference between the simulation and the model reflects the disagreement between the assumption of pressure equilibrium at long distances to the core in LB02b model and the numerical results that display an overpressured co-con by the end of the simulation.

In order to illustrate the discussion in the two previous paragraphs, Fig. 12 shows the jet radius versus distance. The plot clearly shows three regions for the jet morphology as in LB02a,b. The transitions between the inner and flaring regions and between the flaring and outer ones are indicated in the plot. The initial expansion in the inner region, expansion -due to the sudden increase in pressure and density behind the recollimation shock- and contraction in the flaring region, and further expansion of the jet in the outer region, are observed here, as pointed out by LB02a (see their Fig. 4). The oscillations of the jet radius in the outer region are due to the irregularities of the flow. Dotted lines show linear fits of the radius of the jet with respect to distance, that allow to give estimates on local jet opening angles:  $13.8^\circ$  for the inner region,  $4.8^\circ$  for the first half of the flaring region, and  $17.5^\circ$  for the outer one. These values differ from those obtained in LB02a (approximately  $8.5^\circ$ ,  $18.5^\circ$  and  $13.1^\circ$  for the inner, flaring and outer regions, respectively). The



**Table 3.** Shell (shocked ambient medium in the simulation) and ISM (unperturbed ambient medium in the simulation) thermodynamic values in the simulation, compared to those of Centaurus A and NGC 3801. The ranges in the values given for the simulation stand for the different values of the parameters in the transversal and in the axial directions: the maxima (minima) in the shell correspond to the axial (transversal) direction and the maxima (minima) in the ISM correspond to the transversal (axial) direction. The ranges in the other columns are taken from the referenced papers.

|                      | Simulation             | Centaurus A <sup>1</sup> | NGC 3801 <sup>2</sup>  |
|----------------------|------------------------|--------------------------|------------------------|
| $n_{shell} (m^{-3})$ | $(3.3 - 5.2) 10^4$     | $2.0 10^4$               | $(2.0 - 3.0) 10^4$     |
| $n_{ISM} (m^{-3})$   | $(1.4 - 1.5) 10^4$     | $1.7 10^3$               | $4.6 10^3$             |
| $P_{shell} (Pa)$     | $(0.4 - 1.8) 10^{-11}$ | $2.1 10^{-11}$           | $(4.2 - 8.9) 10^{-12}$ |
| $P_{ISM} (Pa)$       | $1.3 10^{-12}$         | $1.0 10^{-13}$           | $3.8 10^{-13}$         |
| $T_{shell} (K)$      | $3.2 10^7 - 1.0 10^9$  | $3.34 10^7$              | $(0.8 - 1.2) 10^7$     |
| $T_{ISM} (K)$        | $1.7 10^7$             | $3.36 10^6$              | $2.67 10^6$            |

<sup>1</sup>Kraft et al. (2003). <sup>2</sup>Croston et al. (2007).

main difference appears in the flaring region and is probably due to the series of recollimation shocks acting in this region in our case. However it should be also pointed out that we measure the radius of the jet using velocity as a reference, whereas LB02a use the emitting material. We have shown in Sec. 3.1 that the jet is radially stratified in the simulation (Fig. 4), so the emitting material could be surrounded by a non-emitting, slower wind that we consider as part of the jet when computing its radius (e.g., gas moving with velocities between  $0.3c$  and  $0.5c$ ).

The jet in the simulation accelerates to a higher velocity (see Fig. 10) than that given in LB02a,b for the jet in the transition from the inner to the flaring region. In the numerical simulation, the jet is injected into the grid with the speed given in LB02b for the jet in the inner region ( $0.87c$ ), and acceleration down the pressure gradient speeds up the jet to  $\sim 0.98c$ . The differences in velocity of the flow and position of the shocks were studied by means of three additional simulations with different values for velocity and pressure ratio with the external medium at injection: Simulation 2, with  $v_j = 0.5c$  and  $P_j/P_{a,c} = 3.8$ ; Simulation 3, with  $v_j = 0.6c$  and  $P_j/P_{a,c} = 7.8$ , and Simulation 4, with  $v_j = 0.5c$  and  $P_j/P_{a,c} = 1$ . In simulations 2 and 3 the first recollimation shock occurs at  $z \sim 700 - 800$  pc, too close to the source compared to observations, due to the smaller velocity (simulations 2 and 3) and smaller pressure ratio with respect to the ambient medium at injection (simulation 2). This result points towards the values used in simulations 1 (main simulation) and 3 for jet overpressure ( $P_j/P_{a,c} \sim 8$ ) and speed at injection ( $v_j \sim 0.6 - 0.87$ ) at  $z \sim 500$  pc to be close to those in the real jet in 3C 31, as we are able to reproduce the transition between the inner and the flaring regions at about the appropriate distances, given in LB02b. Fine tuning of the initial jet velocity and pressure ratio with the external medium can certainly reproduce the exact observed position of the standing shock in the jet in 3C 31. As we have already pointed out, the significant overpressure of the jet at  $z \sim 500$  pc is required in order to produce a discontinuity (recollimation shock) in the transition from the inner to the flaring region at the observed position. This is confirmed by results from simulations 2 and 4, which have lower initial values of jet pressure: In simulation 2 the recollimation shock forms too close to the source compared with the observations, and in simulation 4 the jet shows neither significant expansions nor strong recollimation shocks that can explain the increase in emission at the beginning of the flaring region. We have not studied in this work the possible influence of a change in the atmosphere model of Hardcastle et al. (2002). However, any change in the density and pressure gradients would certainly influ-

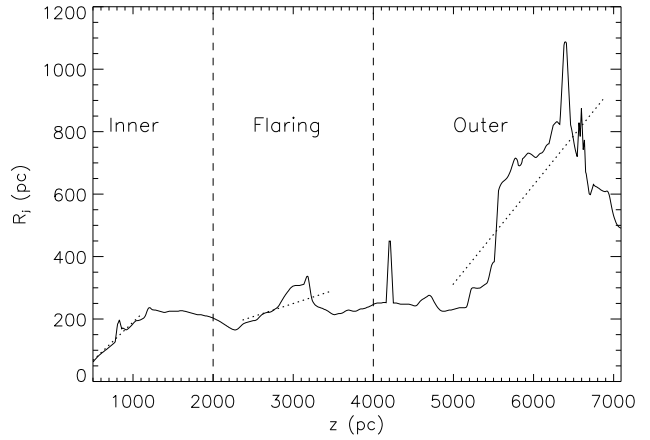


**Figure 12.** Jet radius versus distance in the last frame. Jet radius is computed taking the outermost position where the axial velocity is larger than  $0.3c$ . The boundaries between regions in the simulation are marked with dashed vertical lines; dotted lines indicate fitted parts in order to obtain opening angles.

ence the position of the recollimation shock and the properties of the jet at this point.

#### 4.6 Mass entrainment

From the panel of the tracer distribution at the end of the numerical simulation (Fig. 7), strong mass loading of the flow is observed for distances  $z > 4.5$  kpc. At distances shorter than 4.5 kpc ambient material is entrained through the jet boundary. In the region  $z \sim 4.5 - 6$  kpc the ambient material is entrained by the terminal shock. After this shock, the jet flow is mainly subsonic favouring the entrainment of ambient material. For comparison, in LB02b model, the strongest entrainment occurs at  $z \sim 3 - 3.5$  kpc (see their Fig. 11) downstream the flaring point. After this local maximum in the entrainment rate follows a monotonous increase beyond  $z = 4$  kpc. The authors claim that the mass entrainment is due to stellar mass loss near the flaring point, but due to mixing in a boundary layer farther away. In any case, the comparison between the mass entrainment rate as a function of distance to the source in LB02b model and that derived from our numerical simulation has to be considered with caution, as the simulation has not reached a steady state.

Our simulation allows to conclude that the cause of the discontinuity between the inner and the flaring region and of the process of entrainment in the jets in 3C 31, is the generation of a strong standing shock due to the initial overpressure of the jet, in agreement with LB02b, and not to the growth of Kelvin-Helmholtz instabilities to nonlinear amplitudes (e.g., Rosen & Hardee 2000; Perucho et al. 2005).

## 5 CONCLUSIONS

We present here a hydrodynamical relativistic simulation on the evolution of a FRI jet, using parameters extracted from the modelling that LB02a,b made for the radio jets of 3C 31. The simulated jet is purely leptonic and propagates in a decreasing density and pressure atmosphere with the profiles given in Hardcastle et al. (2002) for 3C 31. The simulation was followed up to  $t = 7.26 \cdot 10^6$  yrs (about one tenth of the estimated lifetime of 3C 31).

The simulation shows that the source can go through a *weak CSS-like* phase in the early evolution. The expansion speed, ages, sizes, and irregular morphologies are in agreement with those claimed by Drake et al. (2004) for low power CSS sources. The further evolution of the simulated jet into an FRI morphology supports their claim that weak CSS sources are the progenitors of large scale FRI jets. Estimates of the age of the source derived from the advance velocities measured in the simulation lead to ages  $t > 10^8$  yrs, in agreement with recent studies of FRI radio galaxies (Parma et al. 2002). The lack of emission gaps in the images points towards 3C 31 having been continuously active since the triggering of its activity phase, with no shorter-term periodicity.

At the end of the simulation, the head of the bow shock has reached a distance of  $\sim 15$  kpc propagating at an almost constant speed of  $7 \cdot 10^{-3} c$  up to  $t = 4.5 \cdot 10^6$  yrs, decelerating afterwards. The region encompassed by the bow shock can be divided in two parts: the cocoon, fed with jet material, hot and light; the shocked ambient medium region, cooler and denser. This structure is reminiscent of the cavity/shell structure characteristic of the shocked regions surrounding powerful jets. The pressure in the shocked region decreases with time with a steeper slope than in the Begelman & Cioffi (1989) model. A simple generalization of this model that takes into account the evolution of the shocked regions in decreasing density atmospheres has been used to explain the fast decrease of pressure as well as the self-similar expansion of the shocked region. Moreover, assuming self-similarity also for the cocoon evolution, our model is able to explain the constant character of temperature in the cocoon with time.

At the end of the simulation, the bow shock is still slightly supersonic (Mach number  $\sim 2.5$ ). This result is supported by recent observations of bow shocks with Mach numbers between 3 and 8 in the low power radio galaxies Centaurus A (Kraft et al. 2003) and NGC 3801 (Croston et al. 2007). The fact that the jet power used in our simulation for the jets in 3C 31 is in the upper part of the range appropriate for FRI sources could explain the presence of a bow shock in the simulation at larger distances from the galaxy than observed in these galaxies. We show that the pressure and number density jumps across the bow shock in the simulation are consistent with those given in Kraft et al. (2003) and Croston et al. (2007) for Centaurus A and NGC 3801, respectively. From this fact, we conclude that the jet in 3C 31 possibly went through the same stage as that observed for those sources, and that the deceleration and disappearance of the bow shock should occur at later times than those simulated here. A possible overestimate of the bow shock pressure

and velocity could be caused by the lack of radiation cooling in the simulation.

Focussing on the jet structure and dynamics, the simulation reveals that the jet expands in the pressure gradient and undergoes several subsequent recollimation and expansion processes that end up in the formation of a wide shear layer, mass loading and complete disruption of the flow. The parameters used in this simulation succeed in explaining the general structure of the jet, as modelled by LB02b. However, the exact locations of transition between model regions in LB02b are not reproduced here. The internal shocks in the simulated jet are formed at different positions than given by the model. Also, the model predicts only one discontinuity in the transition between the inner and flaring regions, and a smooth transition from the flaring to the outer region, whereas we find two more discontinuities in the jet, the latter being the transition from the flaring to the outer region in the simulation. This difference may be caused by the assumption of pressure equilibrium at long distances ( $z \sim 12$  kpc) made in the modelling of LB02b. It should be also kept in mind that our simulation has not reached a steady state. This assumption is validated by the fact that the jets in 3C31 show no lobes, although these jets could have been overpressured as they went through the initial stages simulated here, as it happens with the jets in younger sources like 3C 296 (Laing et al. 2006). The extra discontinuities captured by the simulation are a consequence of the oscillations of the jet around pressure equilibrium with the external medium, that turn out to be stronger than given by LB02b. Fine tuning of the injection velocity ( $v_j \sim 0.6 - 0.87 c$ ) and a significant overpressure of the jet (as that used in our simulation,  $P_j/P_{a,c} \sim 8$ ) are required at injection in the grid ( $z \sim 500$  pc) in order to fit the first recollimation shock to the position given in LB02b. We conclude that a standing shock formed due to the initial overpressure of the jet is the cause for the discontinuity found between the inner and the flaring regions and for the mass entrainment of the jets in 3C 31.

The simulation presented here confirms the paradigm for the evolution of FRI's (Bicknell 1984; Komissarov 1990a,b; Laing 1993, 1996), in which the adiabatic expansion of an overpressured jet is followed by subsequent recollimation in shocks and expansion processes. The jet is decelerated to transonic and subsonic velocities in these shocks, and a mixing layer is formed that finally disrupts the flow. However, recent X-ray observations and this simulation indicate the existence of bow shocks still in kiloparsec scale FRI jets. Further two and three-dimensional magnetohydrodynamic simulations, including radiative cooling and realistic mass entrainment from stellar mass losses should be performed in order to disentangle the role of these processes in the structure and dynamics of the FRI jets. It is important to note that these simulations can be crucial for a deeper understanding not only of the evolution of jets in FRI radio galaxies, but also of their impact on the interstellar and intergalactic media, e.g., through heating.

## ACKNOWLEDGEMENTS

Calculations for this paper were performed on the SGI Altix 3000 computer *CERCA* at the *Servei d'Informàtica de la Universitat de València*. This work was supported in part by the Spanish *Dirección General de Enseñanza Superior* under grants AYA2001-3490-C02-01 and AYA2004-08067-C03-01 and *Conselleria d'Empresa, Universitat i Ciència de la Generalitat Valenciana* under project GV2005/244. M.P. benefited from a postdoctoral fellowship in the Max-Planck-Institut für Radioastronomie in Bonn and a postdoc-

toral fellowship of the *Generalitat Valenciana (Beca Postdoctoral d'Excel·lència)*. The authors want to thank J. Ferrando for useful information on the calculation of the equation of state, T. Beckert and the referee of the paper, R. Laing, for their constructive criticism and useful comments.

## REFERENCES

- Aloy, M.A., Ibáñez, J.M<sup>a</sup>, Martí, J.M<sup>a</sup>, Gómez, J.L., Müller, E. 1999, *ApJL*, 523, 125
- Begelman, M.C., Cioffi, D.F. 1989, *ApJL*, 345, 21
- Bicknell, G.V. 1984, *ApJ*, 286, 68
- Bicknell, G.V. 1994, *ApJ*, 422, 542
- Bicknell, G.V. 1995, *ApJS*, 101, 29
- Bowman, M. 1994, *MNRAS*, 269, 137
- Bowman, M., Leahy, J.P., Komissarov, S.S. 1996, *MNRAS*, 279, 899
- Canvin, J.R., Laing, R.A., 2004, *MNRAS*, 350, 1342
- Canvin, J.R., Laing, R.A., Bridle, A.H., Cotton, W.D. 2005, *MNRAS*, 363, 1223
- Croston, J.H., Kraft, R.P., Hardcastle, M.J. 2007, *astro-ph/0702094*
- de Berredo-Peixoto, G., Shapiro, I.L., Sobreira, F. 2005, *Mod. Phys. Lett. A*, 35, 2723
- De Young, D.S. 1986, *ApJ*, 307, 62
- De Young, D.S. 1993, *ApJL*, 405, 13
- Drake, C.L., Bicknell, G.V., McGregor, P.J., Dopita, M.A. 2004, *AJ*, 128, 969
- Falle, S.A.E.G., Komissarov, S.S. 1996, *MNRAS* 278, 586
- Fanaroff, B.L., Riley, J.M. 1974, *MNRAS*, 167, 31
- Fanti, C., Fanti, R., Dallacasa, D., Schilizzi, R.T., Spencer, R.E., Stanghellini, C. 1995, *A&A*, 302, 317
- Feretti, L., Perley, R., Giovannini, G., Andernach, H. 1999, *Mem. S. A. It.*, 70, 1
- Hardcastle, M.J., Worrall, D.M., Birkinshaw, M., Laing, R.A., Bridle, A.H. 2002, *MNRAS*, 334, 182
- Hardcastle, M.J., Worrall, D.M., Birkinshaw, M., Laing, R.A., Bridle, A.H. 2005, *MNRAS*, 358, 843
- Katz-Stone, D.M., Rudnick, L. 1997, *ApJ*, 488, 146
- Kino, M., Kawakatu, N., Ito, H. 2007, *MNRAS*, 376, 1630
- Komissarov, S.S. 1990a, *Ap&SS*, 165, 313
- Komissarov, S.S. 1990b, *Ap&SS*, 165, 325
- Komissarov, S.S. 1994, *MNRAS*, 269, 394
- Komissarov, S.S., Falle, S.A.E.G. 1998, *MNRAS*, 297, 1087
- Komossa, S., Böhringer, H. 1999, *A&A*, 344, 755
- Kraft, R.P., Vázquez, S.E., Forman, W.R., Jones, C., Murray, S.S., Hardcastle, M.J., Worrall, D.M., Churazov, E. 2003, *ApJ*, 592, 129
- Krause, M., Camenzind, M. 2003, *astro-ph/0307152*
- Krause, M. 2005, *A&A*, 431, 45
- Kunert-Bajraszewska, M., Marecki, A., Thomasson, P., Spencer, R.E. 2005, *A&A*, 440, 93
- Laing, R.A. 1993, in *Astrophysical Jets*, eds. Burgarella, Livio, O'Dea, Cambridge Univ. Press, p. 95
- Laing, R.A. 1996, in *Proceedings of the 175th IAU Symp.*, eds. Eckers, Fanti, Padrielli, Kluwer, p. 147
- Laing, R.A., Bridle, A.H. 2002a, *MNRAS*, 336, 328
- Laing, R.A., Bridle, A.H. 2002b, *MNRAS*, 336, 1161
- Laing, R.A., Bridle, A.H. 2004, *MNRAS*, 348, 1459
- Laing, R.A., Canvin, J.R., Bridle, A.H., and Hardcastle, M.J. 2006, *MNRAS* 372, 510
- Martí, J.M<sup>a</sup>, Müller, E., Font, J.A., Ibáñez, J.M<sup>a</sup>, and Marquina, A. 1997, *ApJ*, 479, 151
- Parma, P., Murgia, M., de Ruiter, H.R., Fanti, R. 2002, *NewAR*, 46, 313
- Perucho, M., Martí, J. M. 2002, *ApJ*, 568, 639
- Perucho, M., Martí, J. M., Hanasz, M. 2004, *A&A*, 427, 431
- Perucho, M., Martí, J. M., Hanasz, M. 2005, *A&A*, 443, 863
- Rosen, A., Hardee, P.E. 2000, *ApJ*, 542, 750
- Scheck, L., Aloy, M.A., Martí, J.M<sup>a</sup>, Gómez, J.L., Müller, E. 2002, *MNRAS*, 331, 615
- Service, A.T. 1986, *ApJ*, 307, 60
- Synge, J.L. 1957, *The relativistic gas*, North-Holland, Amsterdam
- Worrall, D.M., Birkinshaw, M., Laing, R.A., Cotton, W.D., Bridle, A.H. 2007, *MNRAS*, 380, 2
- Zanni, C., Bodo, G., Rossi, P., Massaglia, S., Durbala, A., Ferrari, A. 2003, *A&A*, 402, 949

## APPENDIX A: THE EQUATION OF STATE

The equation of state of a relativistic perfect gas can be written in the form (Synge 1957; Falle & Komissarov 1996):

$$w = \sum_{I=1}^N n_I m_I G(\xi_I), \quad (A1)$$

$$p = \sum_{I=1}^N n_I m_I \xi_I^{-1}, \quad (A2)$$

where,  $w = \rho h$ , with  $\rho$  the proper rest-mass density and  $h$  the specific enthalpy,  $p$  is the pressure,  $n_I$  is the number density of a given family of particles with mass  $m_I$ ,

$$\xi_I = \frac{m_I}{k_B T}, \quad (A3)$$

and

$$G(\xi) = \frac{K_2(\xi)}{K_3(\xi)} = \frac{K_1(\xi)}{K_2(\xi)} + \frac{4}{\xi}. \quad (A4)$$

In the latter equations  $k_B$  is the Boltzmann constant,  $T$ , the temperature and  $K_\nu(\xi)$  are the modified Bessel functions:

$$K_\nu(\xi) = \int_0^\infty \exp(-\xi \cosh \theta) \cosh \nu \theta d\theta. \quad (A5)$$

The adiabatic exponent is derived from the definition of sound speed

$$a^2 = \frac{1}{h} \left( \frac{\partial p}{\partial \rho} \right)_s, \quad (A6)$$

and turns out to be:

$$\Gamma = \frac{\sum_{I=1}^N n_I G'(\xi_I) \xi_I^2}{\sum_{I=1}^N n_I (G'(\xi_I) \xi_I^2 + 1)}, \quad (A7)$$

where  $G'$  represents the derivative of the function with respect to its argument,  $\xi_I$ .

In our case, we deal with two species of particles: leptons (electrons and positrons) and baryons (protons). From the leptonic and total proper rest-mass densities ( $\rho$  and  $\rho_l$ , respectively), charge neutrality allows to obtain the proton rest-mass density,  $\rho_p$ , and the corresponding number densities,  $n_l$  and  $n_p$  (and mass fractions,  $X_l$  and  $X_p$ ). Then,

$$w = \rho_l G(\xi_l) + \rho_p G(\xi_p), \quad (\text{A8})$$

and

$$p = \rho_l \xi_l^{-1} + \rho_p \xi_p^{-1}. \quad (\text{A9})$$

Now, these two last equations together with the equations defining the set of conserved variables, eqs. (6)-(9), form an implicit system from which the values of  $\rho$ ,  $\rho_l$ ,  $p$ ,  $w$ ,  $T$  and the two components of flow velocity,  $v^R$  and  $v^z$ , can be derived. With this purpose, an iteration in the temperature is performed at each numerical cell in every time-step.

Finally,

$$\Gamma = \frac{n_l G'(\xi_l) \xi_l^2 + n_p G'(\xi_p) \xi_p^2}{n_l (G'(\xi_l) \xi_l^2 + 1) + n_p (G'(\xi_p) \xi_p^2 + 1)}, \quad (\text{A10})$$

is the adiabatic exponent.